Molecular Cell

Article

Metamorphic proteins at the basis of human autophagy initiation and lipid transfer

Graphical abstract

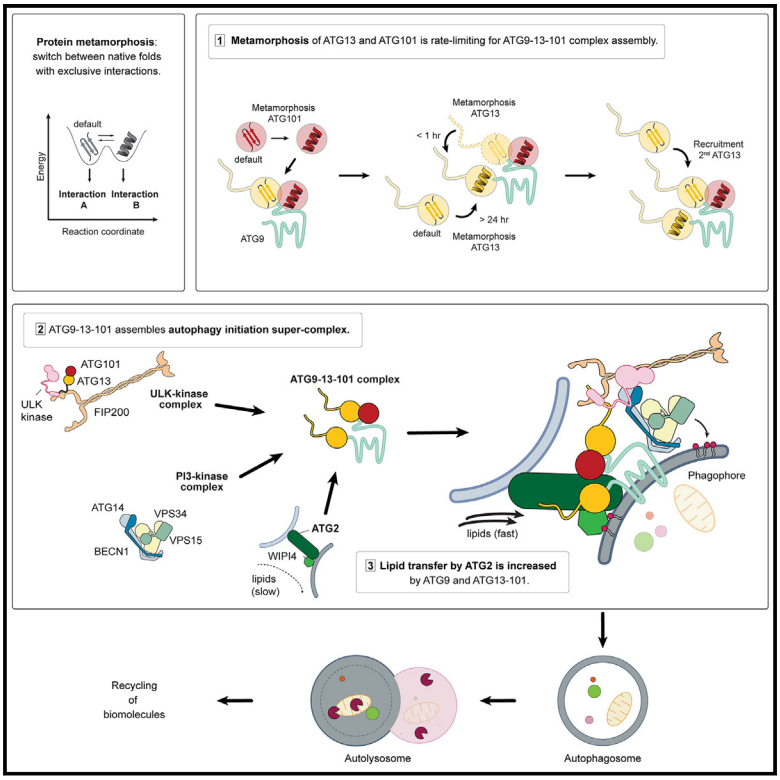

Highlights

- Purified autophagy initiation subcomplexes self-assemble in a supercomplex
- ATG9-13-101 is an assembly platform of supercomplex by recruiting each subcomplex
- Metamorphosis of ATG13 and ATG101 is rate limiting for ATG9-13-101 assembly
- Lipid transfer by ATG2 is accelerated by ATG9 and ATG13-101

Authors

Anh Nguyen, Francesca Lugarini, Céline David, ..., Michael Meinecke, Björn Stork, Alex C. Faesen

Correspondence

alex.faesen@mpinat.mpg.de

In brief

Nguyen et al. report the discovery of a human autophagy initiation supercomplex and its biochemical reconstitution using purified proteins. They find that both its assembly and its lipid transfer are regulated by the rare metamorphosis of two of its components ATG13 and ATG101.

Nguyen et al., 2023, Molecular Cell *83*, 2077–2090
June 15, 2023
https://doi.org/10.1016/j.molcel.2023.04.026

CellPress

Molecular Cell

CellPress
OPEN ACCESS

Article

Metamorphic proteins at the basis of human autophagy initiation and lipid transfer

Anh Nguyen,[1,7] Francesca Lugarini,[1,7] Céline David,[2] Pouya Hosnani,[3,4] Çağla Alagöz,[1] Annabelle Friedrich,[2] David Schlütermann,[2] Barbora Knotkova,[3,4] Anoshi Patel,[1] Iwan Parfentev,[5] Henning Urlaub,[5,6] Michael Meinecke,[3,4] Björn Stork,[2] and Alex C. Faesen[1,8,*]

[1]Max-Planck Institute for Multidisciplinary Sciences, Laboratory of Biochemistry of Signal Dynamics, Göttingen, Germany
[2]Institute of Molecular Medicine I, Medical Faculty and University Hospital Düsseldorf, Heinrich Heine University, Düsseldorf, Germany
[3]Heidelberg University Biochemistry Center (BZH), Heidelberg, Germany
[4]University Medical Centre Göttingen, Department of Cellular Biochemistry, Göttingen, Germany
[5]Max-Planck Institute for Multidisciplinary Sciences, Bioanalytical Mass Spectrometry, Göttingen, Germany
[6]University Medical Centre Göttingen, Institute of Clinical Chemistry, Bioanalytics Group, Göttingen, Germany
[7]These authors contributed equally
[8]Lead contact
*Correspondence: alex.faesen@mpinat.mpg.de
https://doi.org/10.1016/j.molcel.2023.04.026

SUMMARY

Autophagy is a conserved intracellular degradation pathway that generates *de novo* double-membrane autophagosomes to target a wide range of material for lysosomal degradation. In multicellular organisms, autophagy initiation requires the timely assembly of a contact site between the ER and the nascent autophagosome. Here, we report the *in vitro* reconstitution of a full-length seven-subunit human autophagy initiation supercomplex built on a core complex of ATG13-101 and ATG9. Assembly of this core complex requires the rare ability of ATG13 and ATG101 to switch between distinct folds. The slow spontaneous metamorphic conversion is rate limiting for the self-assembly of the supercomplex. The interaction of the core complex with ATG2-WIPI4 enhances tethering of membrane vesicles and accelerates lipid transfer of ATG2 by both ATG9 and ATG13-101. Our work uncovers the molecular basis of the contact site and its assembly mechanisms imposed by the metamorphosis of ATG13-101 to regulate autophagosome biogenesis in space and time.

INTRODUCTION

Macro-autophagy ("autophagy" hereafter) is an essential biological process of regulated degradation that promotes organismal health and longevity and helps combat cancer and neurodegenerative diseases.[1] Autophagy collects cellular macromolecules as cargoes, including large aggregates and even organelles. The process is initiated by the nucleation of a flat membrane cisterna, termed "isolation membrane" or "phagophore," which then expands to surround the cargo and eventually closes to form the double-membrane autophagosome, which then fuses with the lysosome for the final degradation.

Many aspects of the nucleation and growth of the phagophore membrane remain enigmatic.[2] The phagophore is formed at membrane sites, such as the endoplasmic reticulum (ER), ER-mitochondria contact sites, the ER-Golgi intermediate compartment, the plasma membrane (PM), and the Golgi apparatus.[3–7] The current view is that specialized regions of the ER ("omegasomes"), sometimes with intricate membrane-contact sites together with other intracellular organelles, can provide a platform for autophagosome biogenesis.[8] After the induction of autophagy, a complex array of proteins promptly co-localize at the contact sites using unknown mechanisms (Figure 1A). The early events of autophagy initiation involve three main protein components: the ULK complex (consisting of ULK1 or -2 kinase, FIP200, and the HORMA-domain proteins ATG13-101), class III PI3-kinase complex I (VPS34, VPS15, BECN1, and ATG14), and the trimeric transmembrane protein ATG9, a lipid scramblase that resides in highly dynamic small vesicles.[9–14] These ATG9-containing vesicles could provide the membrane seed of the phagophore[15] or could transiently make contact to deliver the components of the autophagy machinery.[12,16,17] ATG9 vesicle recruitment coincides with ATG2 recruitment to the phagophore,[18] which could be part of a larger complex defining the ER-phagophore contact site.[19,20] ATG2 resides predominantly at the ER-phagophore contact sites[21] and is required to form contact sites together with ATG9.[19,22] Together with the PI3P-sensing adaptor protein WIPI4, ATG2 is believed to form the initial membrane tether to allow for lipids to flow into the growing autophagosome.[21,23–25] Interactions between subcomplexes,

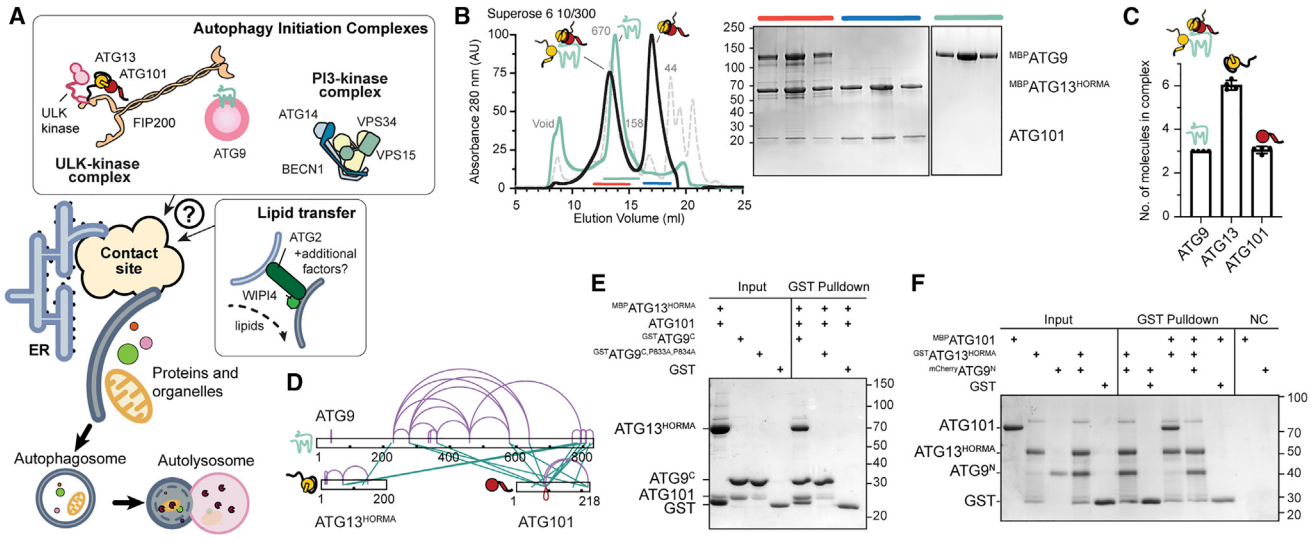

Figure 1. Reconstitution of ATG9-13-101 core complex

(A) The putative coalescence of early autophagy initiation complexes into a supercomplex at the ER contact site promotes the *de novo* formation of an autophagosome.

(B) ATG9, ATG13, and ATG101 form a stable complex. SEC profile of a complex of ^{MBP}ATG9-^{MBP}13^{HORMA}-101 (red line) and an excess of the ^{MBP}ATG13^{HORMA}-101 complex (blue line) with corresponding fractions analyzed by SDS-PAGE.

(C) Quantification of tryptophan fluorescence shows a 3:6:3 stoichiometry of the ATG9-13-101 complex. Error bars represent SD (n = 3 independent experiments).

(D) Crosslinking coupled with mass spectrometry shows a network of crosslinked residues between ATG9 and ATG13-101.

(E) ATG13-101 interacts with ATG9^{C}, which is lost after introducing P833A and P834A point mutants. ATG9^{C} (5 μM) and ATG13-101 (30 μM) were incubated at 4°C for 1 h before pull-down.

(F) ATG101 does not interact with the ATG9^{N}-ATG13^{HORMA} complex. Pull-down performed after 1 h incubation at 4°C using 2 μM bait and 6 μM prey.

See also Figure S1.

like ATG9 with ATG13-101[26,27] and ATG2[19,28] or ATG13 with ATG14,[29,30] have been found, but molecular details are lacking. It is unclear how these subcomplexes cooperate to form a functional contact site, how a stable contact site supercomplex is assembled and disassembled, and how the different parts cooperate to perform the function of the contact site. To shed light on these questions, we embarked on an effort to biochemically reconstitute the human initiation complexes *in vitro* with purified components.

RESULTS

Reconstitution of the ATG9-13-101 complex

The interaction between the ULK1 complex and ATG9 is one of the most upstream events in autophagy. To understand the molecular details of the interaction between the ULK-kinase-complex subunits ATG13-101 and ATG9, we purified the individual full-length proteins and the HORMA domain of ATG13 (ATG13^{HORMA}) (Figures S1A–S1D). We determined the stoichiometry of ATG13-101 and ATG9 using mass photometry, which confirmed that ATG13 and ATG101 form a stoichiometric complex, while ATG9 is a trimer[9,31] (Figures S1I and S1J). Mixing ATG9 with an excess of the ATG13-101 complex resulted in a stable ATG9-13-101 complex (Figures 1B and S1E). The ATG9-13-101 complex partly dissociated in subcomplexes at low concentrations, which prevented us to determine its stoichiometry using mass photometry. We therefore stabilized the complex with 0.01% glutaraldehyde for 1 h at 4°C. This treatment did not change the stoichiometry or the stability of either ATG13-101 or ATG9 (Figures S1K and S1L). Using this protocol, we measured a molecular weight of 998 kDa for the ATG9-13-101 complex, which would indicate a 3:6:3 stoichiometry (Figure S1M). We confirmed this stoichiometry using the stain-free method (Figures 1C, S1N, and S1O).[32] This stoichiometry suggests a complicated assembly mechanism where the ATG13-101 dimer does not interact "en bloc." We observed that both ATG13 and ATG101 individually interact stoichiometrically with ATG9 (Figures S1G, S1H, and S1P). Crosslinking experiments coupled with mass spectrometry, showed that both ATG101 and ATG13 crosslink with the C-terminal portion of ATG9 (Figures 1D, S1A, and S1F; Table S1). A structural model predicted by Alphafold2[33] shows that ATG9 residues 831–839 interact with both ATG13 and ATG101 (Figures S1Q and S1R). This prediction confirms the recently reported crystal structure of ATG13-101 with a ATG9 peptide.[34] Indeed, a construct that contained this region (ATG9^{C}) interacts with the ATG13-101 dimer and, albeit weaker, to both proteins individually in stoichiometric fashion (Figures 1E and S1S), while the ATG9^{core} transmembrane region could not (Figures S1A and S1T). The interaction to the ATG13-101 dimer was lost when mutating the conserved residues P833 and P834 in ATG9^{C}, in agreement with recent reports (Figures 1D and S1U).[34] Conversely, *Saccharomyces cerevisiae* Atg13 has been reported to interact with the poorly conserved N-terminal region of Atg9.[27] Although we observed no crosslinks

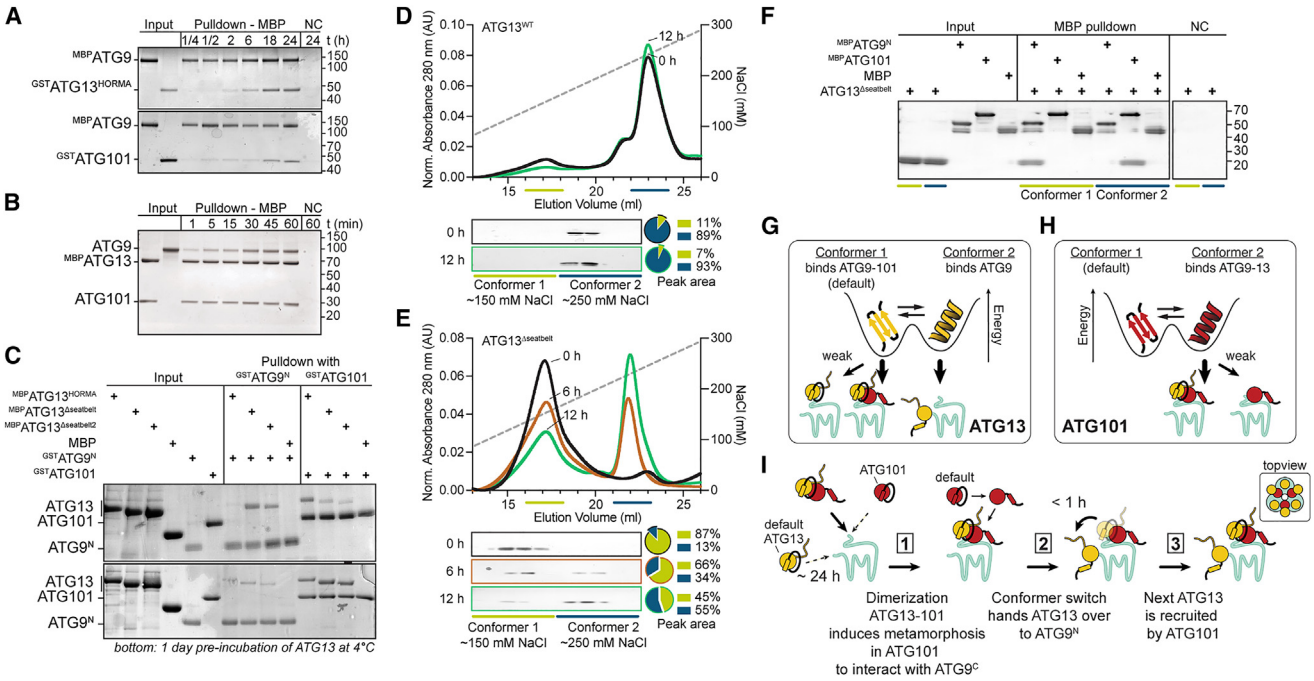

Figure 2. ATG13 and ATG101 metamorphosis dictates assembly of the core complex

(A) Assembly of ATG9-13 (top) and ATG9-101 (below) takes 18–24 h. Pull-down performed after incubation at 20°C for indicated time using 2 μM protein. Negative control (NC) is the last time point without bait.

(B) Assembly of ATG9-13-101 complex takes 30–60 min. Pull-down experiment performed after incubation at indicated times at 4°C using 0.1 μM bait and 0.2 μM prey. Negative control (NC) is the last time point without bait.

(C) ATG13 conformers bind ATG9^{N} or ATG101. ATG13^{WT} quickly interacts with ATG101, while ATG13 mutants default to the ATG9^{N}-binding conformer. After incubation at 4°C without binding partners, the mutants prefer binding to ATG101. Pull-down performed after 1 h incubation using 1 μM bait and 3 μM prey.

(D and E) Anion-exchange chromatography separates two ATG13 conformers. ATG13^{WT} (D) and ATG13$^{\Delta seatbelt}$ (E) elute in distinct peaks. Where ATG13^{WT} defaults to a conformer eluting in peak 2 (~250 mM NaCl), ATG13$^{\Delta seatbelt}$ defaults to a conformer eluting in peak 1 (~150 mM NaCl) while slowly converting to the other conformer.

(F) The ATG13 conformers show differential interaction potential. Pull-down experiment using purified conformers of ATG13$^{\Delta seatbelt}$ (E), showed an interaction to ATG9 ^{N} (conformer 1) or ATG101 (conformer 2), and conversely lose the ability to bind to ATG101 (conformer 1) or ATG9^{N} (conformer 2). Pull-down experiment using 1 μM protein for 10 min at 4°C.

(G and H) Both ATG13 (F) and ATG101 (G) can adopt two conformers with each an exclusive interaction spectrum.

(I) Hand-over assembly model of the ATG9-13-101 complex.

See also Figure S2.

between ATG13 and ATG9^{N}, ATG13 does interact stoichiometrically with ATG9^{N} (Figures S1V and S1W). In contrast, we observed no interaction of ATG101 with ATG9^{N} in pull-down experiments (Figure S1W). However, while ATG101 can interact with ATG13, this interaction was no longer possible when ATG13 was bound to ATG9^{N} (Figure 1F). This shows that the interaction of ATG13 with ATG9^{N} no longer allows for the ATG13-101 dimerization and that ATG13 prefers to bind to ATG9^{N} over ATG101. Overall, the reconstitution of the ATG9-13-101 complex showed stable stoichiometric interactions between ATG9^{C} with both ATG13 and ATG101, as well as the ATG13-101 dimer, while ATG13 also interacts with ATG9^{N}, which prevent simultaneous binding to ATG101 (Figure S1A).

Metamorphosis is rate limiting for ATG9-13-101 assembly

The ability of ATG13 to switch its interaction preference reminded us of a rare property of HORMA-domain proteins. This family of metamorphic proteins can switch between distinct folds (conformers, as opposed to the common conformational changes) at physiological conditions.[35] The emerging paradigm for HORMA-domain proteins is that they default to inactive conformers, before converting to a partner-bound active conformer, thereby regulating the assembly of effector complexes. Switching between conformers involves the unfolding and repositioning of structurally mobile elements to a static core (Figure S1A). Client proteins are typically captured by wrapping their C-terminal "seatbelt" around the interacting client peptide, thereby creating an unusually stable interaction. The considerable energy necessary for metamorphosis could result in slow spontaneous conformer conversions (typically, hours to days). This creates a rate-limiting step in signaling and the assembly (and disassembly) of effector complexes. Indeed, when mixing ATG13 or ATG101 with ATG9, we observed that complex formation was only achieved after an 18- to 24-h incubation at 20°C (Figure 2A). This shows that both ATG13 and ATG101 default

to an inactive non-ATG9-binding state and that a conformer switch is obligatory before interacting with ATG9. In contrast, ATG13 interacts with ATG101 instantaneously, showing that the default conformer of ATG13 requires no metamorphosis to interact with ATG101 (Figure S2A).

Metamorphic proteins frequently can induce conformational switching through dimerization, which can be crucial in accelerating interaction kinetics of HORMA domains with their clients.[35] Since dimerization of ATG13 and ATG101 is essential for autophagy,[36] we wondered if dimerization of ATG13 and ATG101 affects their interaction kinetics with ATG9. Indeed, we observed that their complex formation with $ATG9^{FL}$ or $ATG9^{core+C}$ is accelerated to about 30 min (Figures 2B and S2B). In contrast, the interaction of ATG13 with $ATG9^{N+core}$ is not accelerated by the presence of ATG101 (Figure S2B). This shows that dimerization of ATG13 and ATG101 dramatically accelerates their interaction with $ATG9^{C}$, while the interaction of ATG13 directly with $ATG9^{N}$ remains remarkably slow.

Following a path previously explored with other HORMA domains, we deleted the N- or C-terminal structurally mobile elements of ATG13 with the aim of changing the default conformer.[37] We created ATG13 mutants that lack either the N-terminal ($ATG13^{\Delta N}$) or the C-terminal ($ATG13^{\Delta seatbelt}$) mobile elements, or that contain a shortened internal loop predicted to allow for conformer switching ($ATG13^{LL}$, for "loop-less") (Figure S1A). All these ATG13 mutants lost the ability to bind to ATG101 within 1 h (Figure S2C). However, in presence of ATG101, $ATG13^{\Delta seatbelt}$ slowly converted to an ATG101-binding competent conformer within a few hours (Figure S2A). This suggests that this mutant indeed changed the default conformer state in ATG13. To confirm that ATG13 can indeed adopt two conformer states with differential binding capabilities, we tested the mutants preferential binding to either $ATG9^{N}$ or ATG101 after relatively short incubations (1 h). We observed that $ATG13^{WT}$ prefers to bind to ATG101, while the ATG13 seatbelt mutants preferred $ATG9^{N}$ (Figure 2C, top). This is surprising as it suggests that ATG13 does not require its seatbelt to interact with client proteins, in stark contrast to all other known HORMA-domain proteins. Indeed, removing the seatbelt in ATG13 does not affect its ability to assemble the full ATG9-13-101 complex after prolonged incubations, as judged in pull-down experiments using maltose-binding protein (MBP)-tagged $ATG13^{WT}$ or $ATG13^{\Delta seatbelt}$ (Figure S2D). This suggests that the seatbelt only indirectly contributes to protein interactions and is involved in stabilizing at least one conformer. Removing the seatbelt might therefore be involved in determining the default conformer, but it could additionally affect the rate at which ATG13 switches between conformers. To test this, we used an approach previously used with other metamorphic proteins, where we aimed to induce a conformer switch by incubating the ATG13 constructs overnight at different temperatures in the absence of binding partners.[38,39] Incubating $ATG13^{WT}$ overnight at 4°C did not affect its binding preference, as it still readily bound to ATG101 but not $ATG9^{N}$ (Figure 2C, bottom). In contrast, the ATG13 seatbelt mutants did switch preference from $ATG9^{N}$ to ATG101, suggesting that these mutants can switch between conformer states more easily than $ATG13^{WT}$.

The change in fold upon conformer switching could change the surface charge of the protein, which allows for the separation of individual conformers of some metamorphic proteins, including HORMA-domain proteins, using anion-exchange chromatography.[39–42] We wondered if we could use this approach to purify ATG13 conformers. When eluting $ATG13^{WT}$ from an anion-exchange column using a NaCl gradient, we observed that ATG13 predominantly eluted at roughly 250 mM NaCl (Figure 2D). As expected, the protein eluting in this peak readily binds ATG101, but not $ATG9^{N}$ (Figure S2E). Since we had observed that $ATG13^{\Delta seatbelt}$ more readily switched between conformers (Figure 2C), we repeated the experiment with anion-exchange resin using $ATG13^{\Delta seatbelt}$. We observed that the majority of proteins eluted at a different salt concentration (roughly 150 mM NaCl), suggesting that it eluted as a different conformer (Figure 2E). In agreement with the experiments in Figure 2C, the conformer state of $ATG13^{WT}$ is stable as we did not observe any changes over time in its elution or binding (Figures 2D and S2E). However, the elution of $ATG13^{\Delta seatbelt}$ did again change when incubating the protein at 4°C for prolonged times—which was observed by the disappearance of the peak containing the default conformer ("conformer 1")—and the concomitant appearance of a peak corresponding to the default conformer of $ATG13^{WT}$ ("conformer 2") (Figure 2E). The change in conformer was accompanied by a complete switch in binding behavior. ATG13 eluting in the conformer 1 peak binds to $ATG9^{N}$, but not to ATG101, and this binding behavior is inverted with protein from the conformer 2 peak (Figure 2F). Overall, these experiments show that ATG13 can adopt two structurally different conformers, with each an exclusive binding partner. $ATG13^{WT}$ defaults to a conformer that prefers to bind ATG101, and a slow conformer change is required to bind to $ATG9^{N}$. The ATG13 conformer that binds to $ATG9^{N}$ can no longer interact with ATG101, even without binding to $ATG9^{N}$, which explains the 3:6:3 stoichiometry of the ATG9-13-101 complex.

Overall, these results can be summarized in the following "hand-over model" of the assembly of the ATG9-13-101 complex (Figures 2G–2I). ATG13 and ATG101 can each interact with ATG9, but this requires a slow obligatory conformer switch (~18–24 h) (Figures 2G and 2H). ATG13 defaults to a state that binds ATG101 (Figure 2G), and this dimerization presumably aids ATG101 to change conformer state (Figure 2H). Together they create the composite interface that allows for a fast engagement with $ATG9^{C}$ (Figure 2I, step 1). Here, ATG13 can switch conformer state, and ATG101 "hands over" the ATG13 molecule to $ATG9^{N}$ in about 30 min (at elevated nonphysiological concentrations) (Figures 2G and 2I, step 2). The increased local concentration and proximity might aid in this process, as this step takes many hours without the prior interaction of ATG13-101 with $ATG9^{C}$. Next, ATG101 can recruit another ATG13 to saturate all ATG9 molecules in the trimer (Figure 2I, step 3). This yields a 3:6:3 stoichiometric ATG9-13-101 complex, although substoichiometric amounts of ATG101 might suffice to saturate all $ATG9^{N}$ binding sites with ATG13.

ATG13 and ATG101 metamorphosis controls autophagy in cells

Next, we wondered what consequences the conformer-destabilizing mutants would have in cells. To probe autophagic

CellPress
OPEN ACCESS

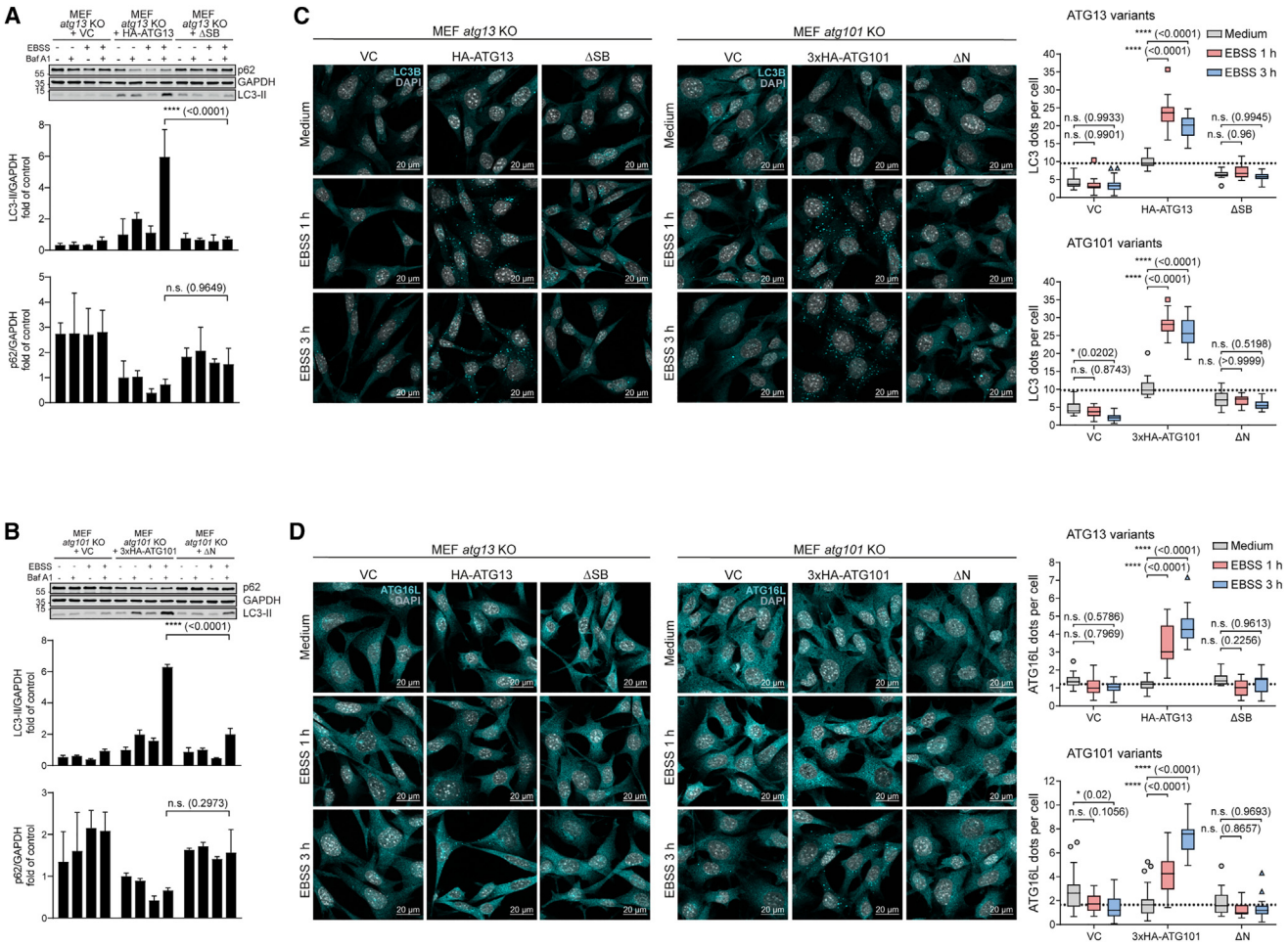

Figure 3. Autophagy is blocked in MEFs expressing conformer-locked ATG13 or ATG101 variants

(A and B) ATG13 and ATG101 conformer mutants decrease basal and starvation-induced LC3 and p62 turnover in MEFs. KO MEFs retrovirally transfected with empty vector (VC) or ATG13 or ATG101 cDNA variants were incubated for 2 h in growth or starvation medium (EBSS) with or without 40 nM bafilomycin A_1. ΔSB, Δseatbelt (see Figure S1A). Results are mean + SD. Statistical analysis used two-way ANOVA (using Tukey's multiple-comparisons test).

(C and D) Cells described in (A) and (B) were grown on glass cover slips overnight and incubated in growth medium (DMEM) or starvation medium (EBSS) for 1 and 3 h. Imaging was performed using a Zeiss Axio Observer 7 fluorescence microscope equipped with a 40×/1.4 Oil DIC M27 Plan-Apochromat objective and ApoTome 2. Representative sections are depicted. Scale bars: 20 μm. The ratio of puncta to cell nuclei of 20 images of three independent experiments is depicted in an interleaved box and whiskers plot (Tukey style). At least 500 cells per condition were analyzed.

See also Figures S3–S5.

degradation activity, we measured autophagic flux in murine embryonic fibroblasts (MEFs).[43] Upon inducing autophagy by Earle's balanced salt solution (EBSS), both LC3 and p62/SQSTM1 turnover were rescued in *atg13* or *atg101* knockout (KO) cells by re-expressing the respective wild-type proteins (Figures 3A and 3B). However, autophagic flux was strongly reduced in cells expressing either ATG13$^{\Delta seatbelt}$ or ATG101$^{\Delta N}$. We also investigated autophagy in these cell lines by immunofluorescence. We monitored endogenous FIP200, phospho-ATG14, WIPI2, ATG16L1, and LC3, thereby examining both early and late stages of autophagosome biogenesis (Figures 3C, 3D, and S3). For all monitored markers, the number of puncta was reduced in cells expressing ATG13$^{\Delta seatbelt}$ or ATG101$^{\Delta N}$ and in the respective KO lines compared with cells expressing ATG13^{WT} or ATG101^{WT}, indicating that the assembly of the autophagy initiation machinery is blocked at an early stage. We also observed that the size of the few remaining LC3 puncta was slightly reduced in ATG13$^{\Delta seatbelt}$ cells compared with wild-type cells. This was also the case for WIPI2 and ATG16L1 puncta in both ATG13$^{\Delta seatbelt}$ and ATG101$^{\Delta N}$-expressing cells, possibly indicating insufficient autophagosome biogenesis.

Next, we aimed to investigate the subcellular localization of ATG13 and ATG9 depending on the ATG13 or ATG101 conformer state, respectively. For that, we made use of HCT116 cells containing a CRISPR-Cas9-mediated knockin of an HA-Tag in frame on the C-terminal end of genomic ATG9A and a simultaneous CRISPR-Cas9-mediated KO of either *ATG13* or *ATG101*.[26] We reconstituted the ATG13 or ATG101 KO cell lines with empty vector or with cDNAs encoding either wild-type or conformer mutants of ATG13 or ATG101

(Figure S5A), and subsequently monitored autophagy-dependent subcellular localization of ATG13 and HA-tagged ATG9 (Figures S4A and S4B). In the *ATG13* KO background (Figure S4A), the numbers of ATG13 puncta increased upon autophagy induction in cells reconstituted with ATG13^{WT}, whereas this effect was clearly reduced in cells expressing ATG13$^{\Delta seatbelt}$. However, the partial co-localization of ATG13 and ATG9 puncta visible for the wild-type variant of ATG13 was not abolished by the introduction of ATG13$^{\Delta seatbelt}$, possibly indicating the capability of this variant to associate with ATG9. Of note, large circular structures of frequently co-localizing ATG9 and ATG13 were occasionally observed in cells expressing ATG13$^{\Delta seatbelt}$, whereas this was not the case for ATG13^{WT}. Similarly, these circular ATG9 structures were seen in the KO background. In the *ATG101* KO background (Figure S4B), ATG13 puncta increased in a starvation-dependent manner only in cells expressing ATG101^{WT}, whereas clear co-localization of ATG13 and ATG9 was already visible in non-starvation conditions in KO or ATG101$^{\Delta N}$-expressing cells. These enlarged ATG9 clusters have been previously described for both ATG13- and ATG101-deficient cells and possibly reflect p62/SQSTM1 clusters or condensates.[26] These clusters were resolved by expressing ATG101^{WT} but not the ATG101$^{\Delta N}$ variant. Accordingly, the observed partial co-localization of ATG13 and ATG9 in *ATG101* KO or ATG101$^{\Delta N}$-expressing cells could indicate binding of "unoccupied" ATG13 to the ATG9 N terminus, but might also be caused by the parallel recruitment of ATG13 and ATG9 to these p62/SQSTM1 clusters. To further address this question, we reconstituted ATG9 expression in *ATG9* KO HCT116[26] by cDNAs encoding either wild-type ATG9, an N-terminally truncated ATG9, a C-terminally truncated ATG9, or ATG9 with a mutated ATG13-101 binding site (P833A, P834A; PAPA) (Figures S4C and S5A). Since the expression levels of the N- and C-terminally truncated ATG9 versions were very low, we did not include them in the analysis by confocal microscopy. We observe enlarged ATG13 puncta in *ATG9* KO cells, again possibly reflecting aggregates caused by stalled autophagy. These structures were resolved by both wild-type ATG9 and the PAPA variant. For the latter, we observed a perinuclear accumulation of ATG9 and qualitatively a reduced overlap with ATG13 after 1 or 3 h of EBSS starvation, indicating an ATG13-binding-dependent ATG9 localization upon autophagy induction.

Since we have shown that the ATG13 mutants affect the conformer states and therefore the interaction with ATG101 *in vitro*, we also investigated the stability of the ULK1 complex in cells. ATG101 was not stabilized in cells expressing ATG13$^{\Delta seatbelt}$, nor were ULK1 and ATG13 stabilized by ATG101$^{\Delta N}$, confirming that these mutants likely abolish the dimerization between ATG13 and ATG101, resulting in the destabilization of the ULK complex (Figure S5B). In cells expressing ATG13$^{\Delta seatbelt}$, ULK1 was stabilized as compared with the parental *atg13* KO MEFs. However, the apparent molecular weight of ULK1 was lower than in cells expressing wild-type ATG13, indicating altered post-translational modifications (Figure S5B). Since we could not exclude that the above-described reduction in autophagic flux was caused by the destabilization and thus reduced expression of components of the ULK1 complex, we re-expressed ATG101 in cells expressing ATG13$^{\Delta seatbelt}$ and analyzed LC3 turnover (Figure S5C). However, LC3 turnover was still clearly reduced in cells expressing ATG13$^{\Delta seatbelt}$ and exogenous ATG101. Of note, ATG101 levels were much more sensitive toward starvation in ATG13$^{\Delta seatbelt}$ cells than in wild-type cells. Furthermore, we observed reduced expression of exogenous ATG101 after several passages (data not shown), indicating that indeed ATG13$^{\Delta seatbelt}$ does not stabilize ATG101.

Since we observed reduced phospho-ATG14 puncta in ATG13$^{\Delta seatbelt}$ and ATG101$^{\Delta N}$ cells, we also monitored ULK1 and ATG14 phosphorylation events by immunoblotting. In cells expressing ATG13$^{\Delta seatbelt}$, inhibitory phosphorylation at ULK1 Ser757 was reduced compared with wild-type ATG13-expressing cells but remained responsive to starvation (Figure S5D, top). This suggests that the autophagy initiation pathway upstream of ULK1 is functional.[44] In contrast, starvation-induced and ULK1-dependent phosphorylation of ATG14 at Ser29 was completely abolished in these cells, confirming the results obtained by immunofluorescence and indicating a defective autophagy signaling downstream of ULK1.[45] Notably, in cells expressing the ATG101$^{\Delta N}$ variant, both ULK1 activation and activity appeared unaffected compared with wild-type ATG101 (Figure S5D, bottom), although this truncation clearly affected autophagic flux. Collectively, these observations suggest that changing the default conformer states of either ATG13 or ATG101 abolishes autophagic flux and prevents the assembly of the early autophagy initiation machinery. Autophagic signaling downstream of ULK1 is most sensitive to mutating ATG13, which strongly reduces binding to ATG101 leading to its instability.

ATG9-13-101 as an interaction hub for supercomplexes

These cellular experiments with ATG13 and ATG101 conformer mutants showed that the assembly of the autophagy initiation machinery is likely blocked at an early stage. Indeed, ATG13 and ATG101 are essential for autophagy and interact with multiple subcomplexes[29,36,46] and are therefore prime candidates to control the putative assembly of a larger initiation machine. Therefore, we asked if an assembled ATG9-13-101 complex could bridge the early autophagy initiation complexes together in stable supercomplexes. To test this, we purified recombinant full-length human ULK1, FIP200, ATG14, and BECN1 (Figures 4A and S6A–S6C). We used mass spectrometry to confirm the identity of all purified proteins (Figure S6M). ATG13-101 could form a stable stoichiometric complex with full-length ULK1 and FIP200 to form the ULK1 complex (Figures 4B and S6D). ATG13-101 also interacted with ATG14-BECN1 (Figures 4B and S6E). When we immobilized ULK1, we could specifically assemble a stable 7-subunit supercomplex containing the ULK1 complex, the ATG9-13-101 complex, and ATG14-BECN1 from the PI3-kinase complex (Figure 4C). We opted to use a preformed ATG9-13-101 complex to ensure that we added a stoichiometric complex. When omitting ATG9-13-101, the supercomplex of early initiation complexes did not form, highlighting the coordinating role of the core complex in the assembly (Figure S6F).

After the initiation complexes, proteins of the autophagosome growth and elongation machinery are recruited in cells (Figure 1A). ATG9 can interact with ATG2, which is proposed to establish membrane-contact sites, together with the ATG2-adapter

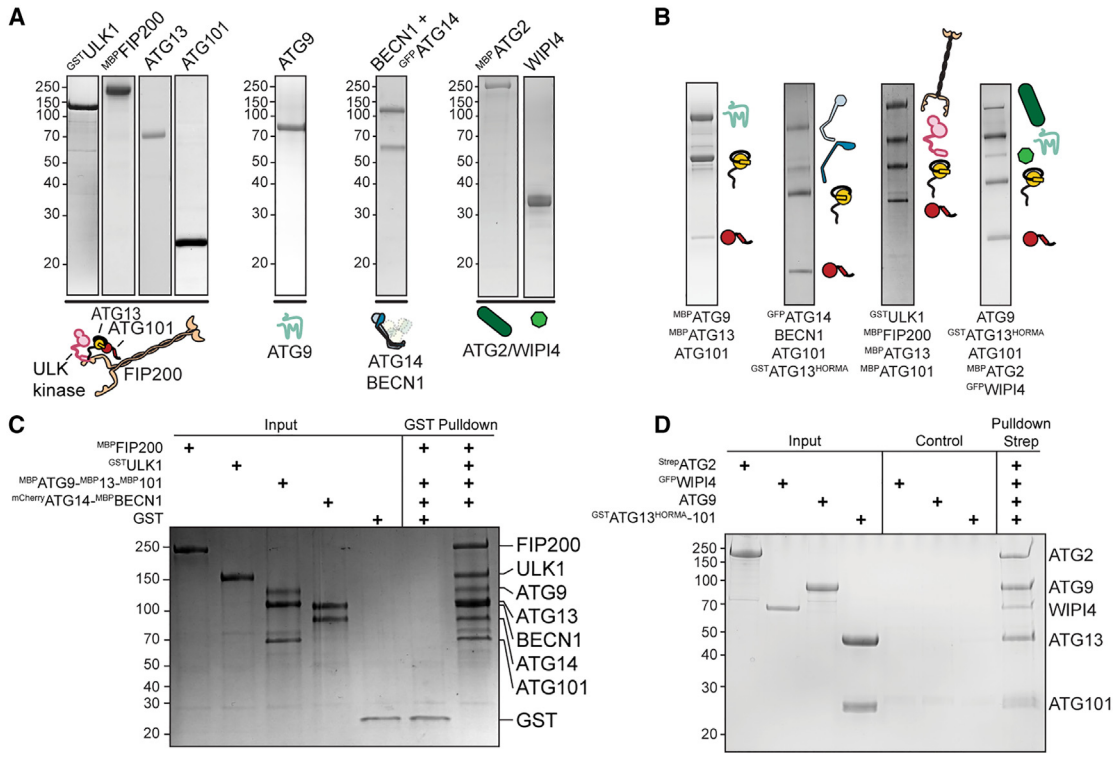

Figure 4. The ATG9-13-101 complex is a core interaction hub for supercomplexes

(A and B) Coomassie-stained SDS-PAGE gallery used in this study of individual recombinant proteins (A) and ATG13-101 containing complexes (B) showing the core ATG9-13-101 complex, the ULK1-kinase complex, the PI3-kinase complex subunits ATG14-BECN1 with the HORMA domains of ATG13-101 and the complex between the ATG9-13-101 core complex and lipid-transfer complex ATG2-WIPI4.

(C) *In vitro* ^{GST}ULK1 pull-down experiment showing a defined 7-subunit complex containing almost all the full-length proteins of the canonical autophagy initiation complexes: ATG9-13-101-FIP200- ULK1-ATG14-BECN1. Pull-down using 1 μM bait and 3 μM prey.

(D) *In vitro* pull-down experiment using ^{strep}ATG2 as bait showing the interaction of ATG2-WIPI4 and ATG9-13-101 in a 5-subunit complex. Pull-down using 1 μM bait and 3 μM prey.

See also Figure S6.

protein WIPI4/Atg18.[19,28,47,48] We therefore wondered if the ATG9-13-101 complex could also accommodate ATG2 and WIPI4. We purified ATG2 and WIPI4, which form a stable complex (Figures 4A and S6G–S6I).[49] While WIPI4 showed no interaction with ATG9 (Figures S6I and S6J), ATG2 could directly interact with both to form a defined complex in pull-down experiments (Figure S6I) as well as in solution (Figure S6K, black). Next, we used ATG2 as a bait to combine all proteins into a 5-subunit ATG2-WIPI4-ATG9-13-101 complex (Figures 4D and S6L). We also note the increased intensity of ATG9-13-101 compared with ATG2-WIPI4, suggesting that an ATG2 monomer likely interacts with an ATG9 trimer, confirming similar reports (Figures 4B and 4D).[20] Overall, this shows that the ATG9-13-101 complex can combine both the ULK1 complex and ATG14-BECN1 of the PI3-kinase complex in a stable supercomplex comprising all canonical initiation complexes, as well as be part of a lipid transfer supercomplex with ATG2/WIPI4.

Increased vesicle tethering and lipid transfer by ATG2

Next, we wondered if the ATG2-WIPI4-ATG9-13-101 complex would affect the membrane tethering and lipid-transfer activity of ATG2. WIPI4 is an ATG2-adapter protein that binds the phospholipid phosphatidylinositol 3-phosphate (PI3P or PtdIns3P), which is part of the lipid signature of autophagic membranes.[50] To visualize membrane binding and tethering by the ATG2-WIPI4 complex using confocal microscopy, we created fluorescently labeled ATG2 and WIPI4. WIPI4 binds strongly and specifically to giant unilamellar vesicles (GUVs) containing PI3P, but we observed no tethering (Figure 5A). Upon addition of ATG2 to WIPI4, we observed a striking clustering of vesicles (Figure 5B, bottom panels) and the establishment of extensive flattened contact between vesicles that show enriched levels of ATG2-WIPI4 (Figure 5B, top panels). We used those conditions to test the ATG2-tethering capabilities of large unilamellar vesicles (LUVs) using dynamic light scattering (DLS). The apparent particle size increased upon adding ATG2, but not when adding ATG9, ATG13-101, WIPI4, FIP200, or ULK1, suggesting that ATG2 is the only membrane tether (Figures S7A and S7B). Adding the nonspecific proteinase K reverted this effect, showing that tethering is reversible and that the increase in particle size is not due to vesicle fusion (Figure S7A). Adding WIPI4 to ATG2 increased the particle size, likely by cooperatively improving the on the weak membrane binding of ATG2 (Figure S7A). Next, we reconstituted ATG9 into protein-free LUVs

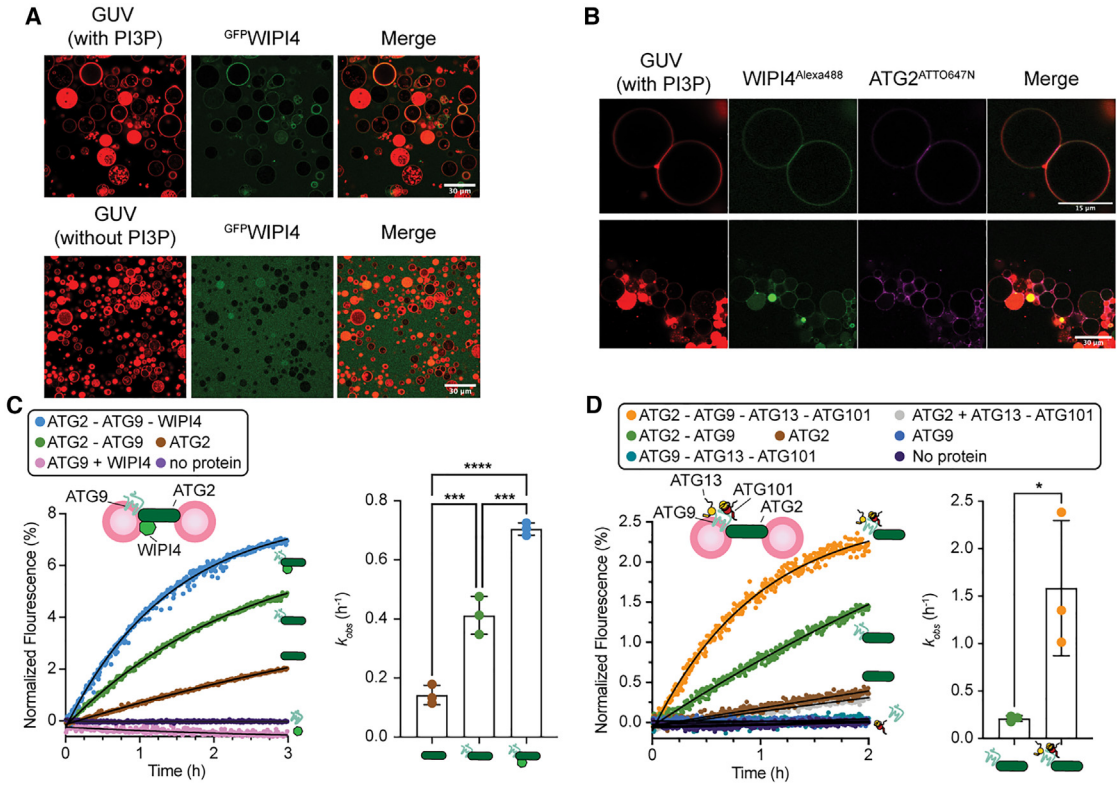

Figure 5. Lipid transfer is accelerated by both ATG9 and ATG13-101

(A and B) Representative images show the membrane localization of lipid-transfer complex ATG2-WIPI4. ^{GFP}WIPI4 (200 nM; green) bound to Rh-GUVs (red) in a PI3P-dependent manner (A). WIPI4 (200 nM; green) and ATG2 (200 nM; purple) cooperate to tether GUVs (red) to form an extensive membrane-contact site (B). Representative images show the tethering of two (top panel) or a cluster of GUVs (bottom panel).

(C) FRET-based lipid-transfer assay showing the effects of ATG9 (100 nM) and WIPI4 (100 nM) on the lipid-transfer efficiency of ATG2 (33 nM). Statistical significance was determined by one-way ANOVA followed by Tukey's multiple-comparisons test. All values are mean ± SD; ***$p < 0.001$; ****$p < 0.0001$. The experiments were performed at 25°C with 3 independent technical replicates. A representative dataset is shown.

(D) ATG13^{HORMA}-ATG101 (100 nM) and ATG9 (100 nM) accelerate lipid transfer by ATG2 (33 nM). Statistical significance was determined by Student's t test. All values are mean ± SD; *$p \leq 0.05$.

The experiments were performed at 25°C with 3 independent technical replicates. A representative dataset is shown. See also Figure S7.

(proteo-liposomes [PLs]) as judged by the flotation of ATG9 to the top fractions of a Nycodenz gradient (Figure S7C). Using a protease protection assay, we observed that the N-terminal MBP tag could be removed from ATG9, indicating that almost all ATG9 was properly oriented in the vesicle bilayer (Figure S7D). Using the ATG9 PLs together with ATG2-WIPI4, we observed a further increase in particle size using DLS, which could be reverted to sizes similar to nontethered LUVs after incubation with proteinase K (Figure S7E). The further addition of FIP200 and ULK1, in the presence of ATP/Mg, did not provide an obvious change in particle size (Figure S7F). Overall, this shows that the ATG2 tethering capabilities are cooperatively enhanced by both ATG9 and WIPI4.

As a peripheral membrane protein, ATG2 mediates lipid transfer between the outer cytosolic membrane leaflets of donor and acceptor vesicles. This results in an asymmetric lipid distribution between the outer and the inner luminal leaflets. The scramblase activity of ATG9 might aid the lipid transfer of ATG2 by re-equilibrating lipids between the leaflets to avoid membrane destabilization.[10,51–53] We confirmed that reconstituted ATG9 in PLs shows robust scramblase activity as judged by the increased levels of bleaching of fluorescently labeled lipids by dithionite compared with ATG9-free liposomes[10,54] (Figure S7G). Dithionite could not bleach nitrobenzoxadiazole (NBD)-labeled glucose inside the vesicles, showing that the ATG9 PLs are closed and that the membrane is impenetrable for dithionite. Therefore, the reduced levels of NBD fluorescence are solely due to ATG9 scramblase activity (Figure S7H). The addition of ATG13-101 to ATG9 did not change the rates or levels of fluorescence bleaching (Figure S7G). All the observed rates of fluorescence decay are fast and comparable, which suggests that the rate of the decrease in fluorescence could be governed by dithionite reactivity and not by the fast ATG9 scramblase activity, consistent with previous observations.[10,47,54,55]

In cells, ATG9 is suggested to reside in the acceptor membrane, while other scramblases reside on the donor membrane on the ER.[47] To test the effect of adding scramblases to membranes, we measured lipid transfer by ATG2 between two ATG9-containing PLs. Using an established assay, donor LUVs are prepared with fluorescent lipids at a concentration sufficient

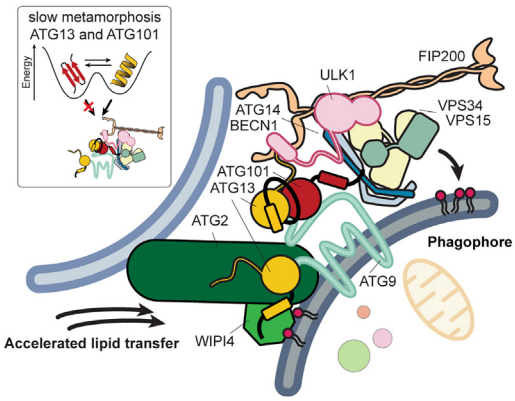

Figure 6. Summary of our findings

All functional subcomplexes form a defined and stable supercomplex. This study finds that the ATG9-13-101 complex is an interaction hub, whose assembly represents a rate-limiting intermediate due to the slow obligatory conversion between topologically distinct native folds of ATG13 and ATG101 (inset). The vesicle tethering and lipid transfer rate of ATG2 is enhanced when interacting with ATG9-13-101.

for FRET (2% NBD-PE and 2% rhodamine-PE) (Figure S7I).[21,24,25] After adding a nonfluorescent acceptor LUV, lipid transfer is quantified by the increase of fluorescence of NBD due to the reduction in FRET after lipids flow between LUVs. The addition of ATG9 increased the lipid-transfer rate of ATG2 by approximately 3 times (with observed rates of 0.14 and 0.4 h^{-1}, respectively), while adding both ATG9 and WIPI4 increased the lipid transfer of ATG2 by approximately 5 times (k_{obs} of 0.7 h^{-1}) (Figure 5C).

The ATG2-WIPI4 and ATG9-13-101 complexes stably interact, but the molecular details of this complex are unclear (Figures 4B, 4D, and S6L). ATG2 interacts in close proximity to the ATG9 lipid entry and exit pores.[20] ATG13 and ATG101 could be crosslinked in the proximity to these ATG9 pores, which suggests they might modulate lipid transfer (Figure 1D). We preassembled the ATG9-13-101 complex by incubating $ATG13^{HORMA}$-101 with ATG9 PLs, before adding ATG2 to start the lipid transfer. Compared with ATG2-ATG9, the presence of ATG13-101 increased the lipid-transfer rate approximately 7.8 times (k_{obs} of 1.57 and 0.2 h^{-1}, respectively) (Figure 5D). In agreement with the vesicle tethering experiments, the further addition of FIP200, ULK1 and ATP/Mg did not affect the lipid transfer by ATG2 (Figure S7J). Similarly, using the ATG13 seatbelt mutant in a preassembled ATG9-13-101 complex does not affect lipid transfer, confirming that formation of the full complex is not affected when using this ATG13 mutant in these conditions (Figure S7K). Overall, this shows that both ATG9 and ATG13-101 cooperatively enhance the lipid-transfer rate of ATG2 by over 20-fold in these conditions.

DISCUSSION

The timely initiation of autophagy is key to maintain the survival of cells under conditions of stress and starvation. In response to starvation, bulk cytosol is taken up within minutes by newly formed autophagosomes. Where autophagosomes initially form and the source of the proteins and lipids needed for autophagosome expansion remain controversial.[8,56] Several membrane-contact sites play an important role in autophagy regulation and progression, which often include a contact between the ER and the phagophore.[8] Analogous contact sites form in yeast between growing autophagosomes and specialized subdomains of the ER called "ER exit sites," where vesicles in the secretory pathway also form.[57,58] Conceptionally, these contact sites can be viewed as performing three distinct but highly integrated functions: (1) they assemble on-demand to create a dynamic interface for the growing autophagosome; (2) they tether the growing autophagosome to distinct ER sites; and (3) they provide ways to incorporate lipids into the growing autophagosome. The composition of the contact site, how it is assembled and disassembled, and the molecular mechanism of its integrated activities are unknown.

This leads to two fundamental questions, both of which are currently incompletely answered. The first question relates to the dynamic composition of the contact site. The induction of autophagy triggers the recruitment of the first "initiating" subcomplexes to the sites of autophagosome biogenesis. In this study, we have presented the purification of two supercomplexes: a 7-subunit supercomplex that stably comprises almost all the full-length proteins of the early human autophagy initiation components (the ULK1 complex, ATG9, and ATG14-BECN1 of the PI3-kinase complex) and a 5-subunit supercomplex of ATG9-13-101 with ATG2/WIPI4 (Figure 6). These stable complexes likely self-assemble in cells in the absence of regulatory mechanisms. Phase separation of the Atg1 kinase complex has been proposed to organize the autophagy machinery, but a similar process is yet to be found in mammalian cells.[59] We found that both supercomplexes share the ATG9-13-101 complex, which serves three functions: (1) the spontaneous but slow metamorphosis of HORMA-domain proteins ATG13 and ATG101 creates an obligatory rate-limiting step in its assembly; (2) it coordinates the co-incidence of all subcomplexes in a stable supercomplex; and (3) it interacts with ATG2-WIPI4 where it enhances vesicle tethering and lipid transfer. It is currently unclear how ATG13-101 aid in vesicle tethering and lipid transfer, but it is likely that they enhance the association of ATG2 with the supercomplex.

The second question, which is strictly related but distinct from the first, regards the triggering event (or rate-limiting step) of supercomplex assembly. The contact site is assembled "on-demand" within minutes after upregulation in starvation-induced autophagy. However, it is unknown what event makes the different functional subgroups abruptly co-localize. Which interaction is the rate-limiting step that would prevent self-assembly? Conversely, upon arrival of the proper signal, the thus far inhibited obligatory intermediate interaction would engage, thereby triggering the self-assembly of the contact site. We show that the interaction between ATG9 and the HORMA-domain proteins ATG13-101 is remarkably slow but key step in the assembly of the supercomplex, which could be the unknown regulated step. Intriguingly, the conformer conversion of HORMA domains can be catalyzed, both at the assembly and disassembly level by a specialized protein machinery.[35,60,61] This presents an enticing and as yet untested possibility that on-demand acceleration of the assembly or disassembly of the

ATG9-13-101 complex could dynamically control contact site assembly and function in space and time. Quantifying the kinetic framework of these interactions, both *in vitro* and in cells, would aid in the identification of these catalysts.

How lipids are transported and delivered to support autophagosome growth remains unclear, but there appear to be three mechanisms by which lipids can reach the growing phagophore: vesicle-mediated delivery; direct extrusion from a preexisting organelle; and direct; protein-mediated transport of lipids.[2] Recent data demonstrating lipid transport by ATG2 support the hypothesis that it facilitates expansion of the phagophore.[62–64] This lipid transport mechanism would support the preferential incorporation of phospholipids synthesized within the ER into phagophore membranes.[65,66] Our work shows that ATG2 requires the cooperative association or the activity of all canonical autophagy initiation subcomplexes: ATG13-101 from the ULK1 complex, ATG9, and the PI3-kinase complex for creating the PI3P lipid signature. This predicts that ATG2 serves as a "co-incidence sensor" for the successful assembly of the supercomplex. This assembled "minimal unit" might then be repeated multiple times to give rise to the "regional" contact sites that support autophagosome growth. However, the incorporation of ATG2-WIPI4 in a larger protein network is not mutually exclusive with a model where additional ATG2 only transiently associates and subsequently diffuses onto the neighboring membranes to create a regional tether. This way, the co-incidence of early autophagy initiation factors is "sensed" as a mature contact site before committing to autophagosome formation.

ATG13 and ATG101 continue to show that most HORMA-domain proteins can reversibly change their protein's three-dimensional structure. Since their ability to engage in protein interactions is exclusive to specific conformers, these proteins directly control the assembly or disassembly of (large) effector complexes. In contrast to other HORMA-domain proteins, neither ATG13 nor ATG101 require their seatbelts to interact with their interaction partners. Nevertheless, removing the seatbelt in ATG13 does change its default conformer state, suggesting that it is used allosterically to regulate interaction interfaces. Disassembling HORMA-domain complexes typically requires a significant amount of energy. This is achieved by remodeling the seatbelt by AAA^{+}-ATPase TRIP13/Pch2 in an ATP-dependent manner, which "opens" the seatbelt leading to the spontaneous disassembly of the effector complex.[67] TRIP13 is a conserved generic HORMA remodeler, but it has not been linked to autophagy. It is therefore currently unclear if the disassembly of the ATG9-13-101 complex and, by extension, the supercomplexes require ATP-dependent remodeling of the HORMA domains to silence autophagosome biogenesis.

In contrast to ATG13, ATG101 is not universally conserved and is most notably missing in *S. cerevisiae*. ATG13 binding to the N terminus of ATG9 is conserved in *S. cerevisiae*,[27] which suggests that this interaction is required for a conserved, but as-yet-undefined function. The exact role of ATG101 is unclear. In mitosis, the "template model" defines two functions for HORMA domain MAD2: a "template" MAD2 acts as an enzyme to convert multiple "copy" MAD2 molecules into the proper conformer to assemble the effector complex.[60] In human autophagy, the "templating" role might be taken up by ATG101 to guide (or "hand over") (Figure 2I) potentially multiple molecules of ATG13 to engage in the functional interaction with ATG9. Species that lack ATG101, could use the MAD2 template mechanism more faithfully where ATG13 serves both roles. Future work will be needed to deconvolute the regulation of this intricate assembly mechanism.

Limitations of the study

While we show that the ATG9-13-101 complex can recruit all other subcomplexes in supercomplexes *in vitro* using purified proteins, a thorough analysis of interactions, complex formation and maturation of cells is required. We present evidence that the assembly of the initiation machinery is dependent on the metamorphic state of ATG13 and ATG101. Purification of endogenous complexes are required to validate this finding and to identify the machinery that could control this metamorphosis in cells. We have been unable to identify conditions or mutants that lock ATG13 or ATG101 in a single conformer state. The retained capacity to switch between conformers limits the deconvolution of the mechanism and contribution of metamorphosis to autophagy initiation in cells and supercomplex assembly. Additionally, more advanced microscopy experiments are needed to visualize the morphological consequences on phagophore nucleation and expansion under conditions of perturbed metamorphosis in cells.

STAR★METHODS

Detailed methods are provided in the online version of this paper and include the following:

- KEY RESOURCES TABLE
- RESOURCE AVAILABILITY
  - Lead contact
  - Materials availability
  - Data and code availability
- EXPERIMENTAL MODEL AND STUDY PARTICIPANT DETAILS
  - *E. coli* strains and media
  - Insect cells and media
  - Cell lines and cell culture
- METHOD DETAILS
  - Reagents & antibodies
  - Expression and purification of proteins
  - Analytical size-exclusion chromatography
  - GST, MBP and Strep pulldown assays
  - Crosslinking with glutaraldehyde
  - Anion exchange chromatography
  - Mass photometry
  - Stain-free protein quantification
  - Preparation of protein-free liposomes
  - Reconstitution of proteins into liposomes
  - Flotation of reconstituted liposome
  - Protease protection assay
  - Leakiness control
  - Lipid transfer assay
  - Scramblase assay

- CXL-MS analysis
- Fluorescence microscopy of liposomes
- Generation of GUVs
- DLS analysis
- Cell lines and cell culture
- Retroviral transduction
- Immunoblotting
- Immunofluorescence

- QUANTIFICATION AND STATISTICAL ANALYSIS

SUPPLEMENTAL INFORMATION

Supplemental information can be found online at https://doi.org/10.1016/j.molcel.2023.04.026.

ACKNOWLEDGMENTS

We thank Noboru Mizushima (University of Tokyo) for kindly providing *atg13* and *atg101* KO MEFs and Joshua L. Andersen (Brigham Young University, Utah) for providing HCT116 ATG9A-HA knockin cells (with additional ATG9 or ATG101 knockout). We thank Anuruti Swarnkar and Claudia Schmidt of the Alex Stein Laboratory (MPI-NAT) for assistance with preparing liposomes and the stain-free protein quantification. We thank Stefanie Asper-Thiel for technical assistance and Laura Griese for establishing the initial ULK1 and FIP200 purification protocols. We thank the Live-Cell Imaging facility (MPI-NAT) for access to the mass photometry equipment, the confocal microscopes and plate reader. We thank the Center for Advanced Imaging (CAi) at the University Düsseldorf for providing access to the Zeiss LSM 880 Airyscan Fast. We are grateful to Reinhard Jahn and Alex Stein for continuous advice over the course of this project, and access to the DLS equipment. This work was supported by Max Planck Society (to A.C.F. and H.U.) and DFG SFB1190 (to A.C.F.). B.S. is supported by the DFG (GRK2158, GRK2578, STO864/4-3, and STO864/6-1). B.K. is supported by the Boehringer Ingelheim Fonds. This work was supported by DFG-INST 208/746-1 FUGG.

AUTHOR CONTRIBUTIONS

A.N., F.L., P.H., C.A., A.P., M.M., and A.C.F. designed *in vitro* experiments and analyzed results. A.N. and F.L. set up recombinant expression systems, established purification protocols, and purified proteins with the help of A.P. A.N., F.L., and C.A., and A.P. performed *in vitro* experiments. C.D., A.C.F., and D.S. performed cellular assays including generation of cell lines, immunoblotting, widefield and confocal fluorescence microscopy—supervised by B.S. A.N., P.H., and C.A. performed vesicle tethering, lipid scramblase and transfer experiments with help from B.K.—supervised by M.M. and A.C.F. I.P. performed mass-spectrometry and analysis, supervised by H.U. A.C.F. wrote the manuscript with input from A.N. and B.S.

DECLARATION OF INTERESTS

The authors declare no competing interests.

INCLUSION AND DIVERSITY

One or more of the authors of this paper self-identifies as a member of the LGBTQIA+ community.

Received: August 31, 2022
Revised: February 23, 2023
Accepted: April 27, 2023
Published: May 19, 2023

REFERENCES

1. Yamamoto, H., Zhang, S., and Mizushima, N. (2023). Autophagy genes in biology and disease. Nat. Rev. Genet. 1–19. https://doi.org/10.1038/s41576-022-00562-w.
2. Melia, T.J., Lystad, A.H., and Simonsen, A. (2020). Autophagosome biogenesis: from membrane growth to closure. J. Cell Biol. *219*. https://doi.org/10.1083/jcb.202002085.
3. Axe, E.L., Walker, S.A., Manifava, M., Chandra, P., Roderick, H.L., Habermann, A., Griffiths, G., and Ktistakis, N.T. (2008). Autophagosome formation from membrane compartments enriched in phosphatidylinositol 3-phosphate and dynamically connected to the endoplasmic reticulum. J. Cell Biol. *182*, 685–701. https://doi.org/10.1083/jcb.200803137.
4. Ge, L., Melville, D., Zhang, M., and Schekman, R. (2013). The ER-Golgi intermediate compartment is a key membrane source for the LC3 lipidation step of autophagosome biogenesis. eLife *2*, e00947. https://doi.org/10.7554/eLife.00947.
5. Hamasaki, M., Furuta, N., Matsuda, A., Nezu, A., Yamamoto, A., Fujita, N., Oomori, H., Noda, T., Haraguchi, T., Hiraoka, Y., et al. (2013). Autophagosomes form at ER-mitochondria contact sites. Nature *495*, 389–393. https://doi.org/10.1038/nature11910.
6. Hayashi-Nishino, M., Fujita, N., Noda, T., Yamaguchi, A., Yoshimori, T., and Yamamoto, A. (2009). A subdomain of the endoplasmic reticulum forms a cradle for autophagosome formation. Nat. Cell Biol. *11*, 1433–1437. https://doi.org/10.1038/ncb1991.
7. Ravikumar, B., Moreau, K., Jahreiss, L., Puri, C., and Rubinsztein, D.C. (2010). Plasma membrane contributes to the formation of pre-autophagosomal structures. Nat. Cell Biol. *12*, 747–757. https://doi.org/10.1038/ncb2078.
8. Ktistakis, N.T. (2020). ER platforms mediating autophagosome generation. Biochim. Biophys. Acta Mol. Cell Biol. Lipids *1865*, 158433. https://doi.org/10.1016/j.bbalip.2019.03.005.
9. Guardia, C.M., Tan, X.F., Lian, T., Rana, M.S., Zhou, W., Christenson, E.T., Lowry, A.J., Faraldo-Gómez, J.D., Bonifacino, J.S., Jiang, J., et al. (2020). Structure of human ATG9A, the only transmembrane protein of the core autophagy machinery. Cell Rep. *31*, 107837. https://doi.org/10.1016/j.celrep.2020.107837.
10. Maeda, S., Yamamoto, H., Kinch, L.N., Garza, C.M., Takahashi, S., Otomo, C., Grishin, N.V., Forli, S., Mizushima, N., and Otomo, T. (2020). Structure, lipid scrambling activity and role in autophagosome formation of ATG9A. Nat. Struct. Mol. Biol. *27*, 1194–1201. https://doi.org/10.1038/s41594-020-00520-2.
11. Mari, M., Griffith, J., Rieter, E., Krishnappa, L., Klionsky, D.J., and Reggiori, F. (2010). An Atg9-containing compartment that functions in the early steps of autophagosome biogenesis. J. Cell Biol. *190*, 1005–1022. https://doi.org/10.1083/jcb.200912089.
12. Orsi, A., Razi, M., Dooley, H.C., Robinson, D., Weston, A.E., Collinson, L.M., and Tooze, S.A. (2012). Dynamic and transient interactions of Atg9 with autophagosomes, but not membrane integration, are required for autophagy. Mol. Biol. Cell *23*, 1860–1873. https://doi.org/10.1091/mbc.E11-09-0746.
13. Yamamoto, H., Kakuta, S., Watanabe, T.M., Kitamura, A., Sekito, T., Kondo-Kakuta, C., Ichikawa, R., Kinjo, M., and Ohsumi, Y. (2012). Atg9 vesicles are an important membrane source during early steps of autophagosome formation. J. Cell Biol. *198*, 219–233. https://doi.org/10.1083/jcb.201202061.
14. Young, A.R., Chan, E.Y., Hu, X.W., Köchl, R., Crawshaw, S.G., High, S., Hailey, D.W., Lippincott-Schwartz, J., and Tooze, S.A. (2006). Starvation and ULK1-dependent cycling of mammalian Atg9 between the TGN and endosomes. J. Cell Sci. *119*, 3888–3900. https://doi.org/10.1242/jcs.03172.
15. Sawa-Makarska, J., Baumann, V., Coudevylle, N., von Bülow, S., Nogellova, V., Abert, C., Schuschnig, M., Graef, M., Hummer, G., and Martens, S. (2020). Reconstitution of autophagosome nucleation defines

Atg9 vesicles as seeds for membrane formation. Science *369*. https://doi.org/10.1126/science.aaz7714.

16. Judith, D., Jefferies, H.B.J., Boeing, S., Frith, D., Snijders, A.P., and Tooze, S.A. (2019). ATG9A shapes the forming autophagosome through Arfaptin 2 and phosphatidylinositol 4-kinase IIIbeta. J. Cell Biol. *218*, 1634–1652. https://doi.org/10.1083/jcb.201901115.

17. Karanasios, E., Walker, S.A., Okkenhaug, H., Manifava, M., Hummel, E., Zimmermann, H., Ahmed, Q., Domart, M.C., Collinson, L., and Ktistakis, N.T. (2016). Autophagy initiation by ULK complex assembly on ER tubulovesicular regions marked by ATG9 vesicles. Nat. Commun. *7*, 12420. https://doi.org/10.1038/ncomms12420.

18. Papinski, D., and Kraft, C. (2014). Atg1 kinase organizes autophagosome formation by phosphorylating Atg9. Autophagy *10*, 1338–1340. https://doi.org/10.4161/auto.28971.

19. Gómez-Sánchez, R., Rose, J., Guimarães, R., Mari, M., Papinski, D., Rieter, E., Geerts, W.J., Hardenberg, R., Kraft, C., Ungermann, C., et al. (2018). Atg9 establishes Atg2-dependent contact sites between the endoplasmic reticulum and phagophores. J. Cell Biol. *217*, 2743–2763. https://doi.org/10.1083/jcb.201710116.

20. van Vliet, A.R., Chiduza, G.N., Maslen, S.L., Pye, V.E., Joshi, D., De Tito, S., Jefferies, H.B.J., Christodoulou, E., Roustan, C., Punch, E., et al. (2022). ATG9A and ATG2A form a heteromeric complex essential for autophagosome formation. Mol. Cell *82*, 4324–4339.e8. https://doi.org/10.1016/j.molcel.2022.10.017.

21. Valverde, D.P., Yu, S., Boggavarapu, V., Kumar, N., Lees, J.A., Walz, T., Reinisch, K.M., and Melia, T.J. (2019). ATG2 transports lipids to promote autophagosome biogenesis. J. Cell Biol. *218*, 1787–1798. https://doi.org/10.1083/jcb.201811139.

22. Kotani, T., Kirisako, H., Koizumi, M., Ohsumi, Y., and Nakatogawa, H. (2018). The Atg2-Atg18 complex tethers pre-autophagosomal membranes to the endoplasmic reticulum for autophagosome formation. Proc. Natl. Acad. Sci. USA *115*, 10363–10368. https://doi.org/10.1073/pnas.1806727115.

23. Chowdhury, S., Otomo, C., Leitner, A., Ohashi, K., Aebersold, R., Lander, G.C., and Otomo, T. (2018). Insights into autophagosome biogenesis from structural and biochemical analyses of the ATG2A-WIPI4 complex. Proc. Natl. Acad. Sci. USA *115*. E9792–E9801. https://doi.org/10.1073/pnas.1811874115.

24. Maeda, S., Otomo, C., and Otomo, T. (2019). The autophagic membrane tether ATG2A transfers lipids between membranes. eLife *8*. https://doi.org/10.7554/eLife.45777.

25. Osawa, T., Kotani, T., Kawaoka, T., Hirata, E., Suzuki, K., Nakatogawa, H., Ohsumi, Y., and Noda, N.N. (2019). Atg2 mediates direct lipid transfer between membranes for autophagosome formation. Nat. Struct. Mol. Biol. *26*, 281–288. https://doi.org/10.1038/s41594-019-0203-4.

26. Kannangara, A.R., Poole, D.M., McEwan, C.M., Youngs, J.C., Weerasekara, V.K., Thornock, A.M., Lazaro, M.T., Balasooriya, E.R., Oh, L.M., Soderblom, E.J., et al. (2021). BioID reveals an ATG9A interaction with ATG13-ATG101 in the degradation of p62/SQSTM1-ubiquitin clusters. EMBO Rep. *22*, e51136. https://doi.org/10.15252/embr.202051136.

27. Suzuki, H., Kaizuka, T., Mizushima, N., and Noda, N.N. (2015). Structure of the Atg101-Atg13 complex reveals essential roles of Atg101 in autophagy initiation. Nat. Struct. Mol. Biol. *22*, 572–580. https://doi.org/10.1038/nsmb.3036.

28. Wang, C.W., Kim, J., Huang, W.P., Abeliovich, H., Stromhaug, P.E., Dunn, W.A., Jr., and Klionsky, D.J. (2001). Apg2 is a novel protein required for the cytoplasm to vacuole targeting, autophagy, and pexophagy pathways. J. Biol. Chem. *276*, 30442–30451. https://doi.org/10.1074/jbc.M102342200.

29. Jao, C.C., Ragusa, M.J., Stanley, R.E., and Hurley, J.H. (2013). A HORMA domain in Atg13 mediates PI 3-kinase recruitment in autophagy. Proc. Natl. Acad. Sci. USA *110*, 5486–5491. https://doi.org/10.1073/pnas.1220306110.

30. Park, J.M., Jung, C.H., Seo, M., Otto, N.M., Grunwald, D., Kim, K.H., Moriarity, B., Kim, Y.M., Starker, C., Nho, R.S., et al. (2016). The ULK1 complex mediates MTORC1 signaling to the autophagy initiation machinery via binding and phosphorylating ATG14. Autophagy *12*, 547–564. https://doi.org/10.1080/15548627.2016.1140293.

31. Qi, S., Kim, D.J., Stjepanovic, G., and Hurley, J.H. (2015). Structure of the human Atg13-Atg101 HORMA heterodimer: an interaction hub within the ULK1 complex. Structure *23*, 1848–1857. https://doi.org/10.1016/j.str.2015.07.011.

32. Gilda, J.E., and Gomes, A.V. (2013). Stain-Free total protein staining is a superior loading control to beta-actin for Western blots. Anal. Biochem. *440*, 186–188. https://doi.org/10.1016/j.ab.2013.05.027.

33. Jumper, J., Evans, R., Pritzel, A., Green, T., Figurnov, M., Ronneberger, O., Tunyasuvunakool, K., Bates, R., Žídek, A., Potapenko, A., et al. (2021). Highly accurate protein structure prediction with AlphaFold. Nature *596*, 583–589. https://doi.org/10.1038/s41586-021-03819-2.

34. Ren, X., Nguyen, T.N., Lam, W.K., Buffalo, C.Z., Lazarou, M., Yokom, A.L., and Hurley, J.H. (2023). Structural basis for ATG9A recruitment to the ULK1 complex in mitophagy initiation. Sci. Adv. *9*, eadg2997. https://doi.org/10.1126/sciadv.adg2997.

35. Gu, Y., Desai, A., and Corbett, K.D. (2022). Evolutionary dynamics and molecular mechanisms of HORMA domain protein signaling. Annu. Rev. Biochem. *91*, 541–569. https://doi.org/10.1146/annurev-biochem-090920-103246.

36. Wallot-Hieke, N., Verma, N., Schlütermann, D., Berleth, N., Deitersen, J., Böhler, P., Stuhldreier, F., Wu, W., Seggewiß, S., Peter, C., et al. (2018). Systematic analysis of ATG13 domain requirements for autophagy induction. Autophagy *14*, 743–763. https://doi.org/10.1080/15548627.2017.1387342.

37. Mapelli, M., and Musacchio, A. (2007). MAD contortions: conformational dimerization boosts spindle checkpoint signaling. Curr. Opin. Struct. Biol. *17*, 716–725. https://doi.org/10.1016/j.sbi.2007.08.011.

38. Mapelli, M., Massimiliano, L., Santaguida, S., and Musacchio, A. (2007). The Mad2 conformational dimer: structure and implications for the spindle assembly checkpoint. Cell *131*, 730–743. https://doi.org/10.1016/j.cell.2007.08.049.

39. Tuinstra, R.L., Peterson, F.C., Kutlesa, S., Elgin, E.S., Kron, M.A., and Volkman, B.F. (2008). Interconversion between two unrelated protein folds in the lymphotactin native state. Proc. Natl. Acad. Sci. USA *105*, 5057–5062. https://doi.org/10.1073/pnas.0709518105.

40. Luo, X., Tang, Z., Xia, G., Wassmann, K., Matsumoto, T., Rizo, J., and Yu, H. (2004). The Mad2 spindle checkpoint protein has two distinct natively folded states. Nat. Struct. Mol. Biol. *11*, 338–345. https://doi.org/10.1038/nsmb748.

41. Sironi, L., Melixetian, M., Faretta, M., Prosperini, E., Helin, K., and Musacchio, A. (2001). Mad2 binding to Mad1 and Cdc20, rather than oligomerization, is required for the spindle checkpoint. EMBO J. *20*, 6371–6382. https://doi.org/10.1093/emboj/20.22.6371.

42. Ye, Q., Lau, R.K., Mathews, I.T., Birkholz, E.A., Watrous, J.D., Azimi, C.S., Pogliano, J., Jain, M., and Corbett, K.D. (2020). HORMA domain proteins and a Trip13-like ATPase regulate bacterial cGAS-like enzymes to mediate bacteriophage immunity. Mol. Cell *77*, 709–722.e7. https://doi.org/10.1016/j.molcel.2019.12.009.

43. Klionsky, D.J., Abdel-Aziz, A.K., Abdelfatah, S., Abdellatif, M., Abdoli, A., Abel, S., Abeliovich, H., Abildgaard, M.H., Abudu, Y.P., Acevedo-Arozena, A., et al. (2021). Guidelines for the use and interpretation of assays for monitoring autophagy (4th edition)1. Autophagy *17*, 1–382. https://doi.org/10.1080/15548627.2020.1797280.

44. Wong, P.M., Feng, Y., Wang, J., Shi, R., and Jiang, X. (2015). Regulation of autophagy by coordinated action of mTORC1 and protein phosphatase 2A. Nat. Commun. *6*, 8048. https://doi.org/10.1038/ncomms9048.

45. Wold, M.S., Lim, J., Lachance, V., Deng, Z., and Yue, Z. (2016). ULK1-mediated phosphorylation of ATG14 promotes autophagy and is impaired

in Huntington's disease models. Mol. Neurodegener. *11*, 76. https://doi.org/10.1186/s13024-016-0141-0.

46. Koyama-Honda, I., Itakura, E., Fujiwara, T.K., and Mizushima, N. (2013). Temporal analysis of recruitment of mammalian ATG proteins to the autophagosome formation site. Autophagy *9*, 1491–1499. https://doi.org/10.4161/auto.25529.
47. Ghanbarpour, A., Valverde, D.P., Melia, T.J., and Reinisch, K.M. (2021). A model for a partnership of lipid transfer proteins and scramblases in membrane expansion and organelle biogenesis. Proc. Natl. Acad. Sci. USA *118*. https://doi.org/10.1073/pnas.2101562118.
48. Tang, Z., Takahashi, Y., He, H., Hattori, T., Chen, C., Liang, X., Chen, H., Young, M.M., and Wang, H.G. (2019). TOM40 targets Atg2 to mitochondria-associated ER membranes for phagophore expansion. Cell Rep. *28*, 1744–1757.e5. https://doi.org/10.1016/j.celrep.2019.07.036.
49. Lu, Q., Yang, P., Huang, X., Hu, W., Guo, B., Wu, F., Lin, L., Kovács, A.L., Yu, L., and Zhang, H. (2011). The WD40 repeat PtdIns(3)P-binding protein EPG-6 regulates progression of omegasomes to autophagosomes. Dev. Cell *21*, 343–357. https://doi.org/10.1016/j.devcel.2011.06.024.
50. Burman, C., and Ktistakis, N.T. (2010). Regulation of autophagy by phosphatidylinositol 3-phosphate. FEBS Lett. *584*, 1302–1312. https://doi.org/10.1016/j.febslet.2010.01.011.
51. Gómez-Sánchez, R., Tooze, S.A., and Reggiori, F. (2021). Membrane supply and remodeling during autophagosome biogenesis. Curr. Opin. Cell Biol. *71*, 112–119. https://doi.org/10.1016/j.ceb.2021.02.001.
52. Noda, N.N. (2021). Atg2 and Atg9: intermembrane and interleaflet lipid transporters driving autophagy. Biochim. Biophys. Acta Mol. Cell Biol. Lipids *1866*, 158956. https://doi.org/10.1016/j.bbalip.2021.158956.
53. Reinisch, K.M., Chen, X.W., and Melia, T.J. (2021). "VTT"-domain proteins VMP1 and TMEM41B function in lipid homeostasis globally and locally as ER scramblases. Contact (Thousand Oaks) *4*. https://doi.org/10.1177/25152564211024494.
54. Matoba, K., Kotani, T., Tsutsumi, A., Tsuji, T., Mori, T., Noshiro, D., Sugita, Y., Nomura, N., Iwata, S., Ohsumi, Y., et al. (2020). Atg9 is a lipid scramblase that mediates autophagosomal membrane expansion. Nat. Struct. Mol. Biol. *27*, 1185–1193. https://doi.org/10.1038/s41594-020-00518-w.
55. Falzone, M.E., and Accardi, A. (2020). Reconstitution of proteoliposomes for phospholipid scrambling and nonselective channel assays. Methods Mol. Biol. *2127*, 207–225. https://doi.org/10.1007/978-1-0716-0373-4_15.
56. Cohen, S., Valm, A.M., and Lippincott-Schwartz, J. (2018). Interacting organelles. Curr. Opin. Cell Biol. *53*, 84–91. https://doi.org/10.1016/j.ceb.2018.06.003.
57. Graef, M., Friedman, J.R., Graham, C., Babu, M., and Nunnari, J. (2013). ER exit sites are physical and functional core autophagosome biogenesis components. Mol. Biol. Cell *24*, 2918–2931. https://doi.org/10.1091/mbc.E13-07-0381.
58. Suzuki, K., Akioka, M., Kondo-Kakuta, C., Yamamoto, H., and Ohsumi, Y. (2013). Fine mapping of autophagy-related proteins during autophagosome formation in Saccharomyces cerevisiae. J. Cell Sci. *126*, 2534–2544. https://doi.org/10.1242/jcs.122960.
59. Fujioka, Y., Alam, J.M., Noshiro, D., Mouri, K., Ando, T., Okada, Y., May, A.I., Knorr, R.L., Suzuki, K., Ohsumi, Y., et al. (2020). Phase separation organizes the site of autophagosome formation. Nature *578*, 301–305. https://doi.org/10.1038/s41586-020-1977-6.
60. De Antoni, A., Pearson, C.G., Cimini, D., Canman, J.C., Sala, V., Nezi, L., Mapelli, M., Sironi, L., Faretta, M., Salmon, E.D., et al. (2005). The Mad1/Mad2 complex as a template for Mad2 activation in the spindle assembly checkpoint. Curr. Biol. *15*, 214–225. https://doi.org/10.1016/j.cub.2005.01.038.
61. Faesen, A.C., Thanasoula, M., Maffini, S., Breit, C., Müller, F., van Gerwen, S., Bange, T., and Musacchio, A. (2017). Basis of catalytic assembly of the mitotic checkpoint complex. Nature *542*, 498–502. https://doi.org/10.1038/nature21384.
62. Dabrowski, R., Tulli, S., and Graef, M. (2023). Parallel phospholipid transfer by Vps13 and Atg2 determines autophagosome biogenesis dynamics. J. Cell Biol. *222*, e202211039. https://doi.org/10.1083/jcb.202211039.
63. Melia, T.J., and Reinisch, K.M. (2022). A possible role for VPS13-family proteins in bulk lipid transfer, membrane expansion and organelle biogenesis. J. Cell Sci. *135*. https://doi.org/10.1242/jcs.259357.
64. Zhang, Y., Ge, J., Bian, X., and Kumar, A. (2022). Quantitative models of lipid transfer and membrane contact formation. Contact (Thousand Oaks) *5*, 1–21. https://doi.org/10.1177/25152564221096024.
65. Orii, M., Tsuji, T., Ogasawara, Y., and Fujimoto, T. (2021). Transmembrane phospholipid translocation mediated by Atg9 is involved in autophagosome formation. J. Cell Biol. *220*. https://doi.org/10.1083/jcb.202009194.
66. Schütter, M., Giavalisco, P., Brodesser, S., and Graef, M. (2020). Local fatty acid channeling into phospholipid synthesis drives phagophore expansion during autophagy. Cell *180*, 135–149.e14. https://doi.org/10.1016/j.cell.2019.12.005.
67. Ye, Q., Rosenberg, S.C., Moeller, A., Speir, J.A., Su, T.Y., and Corbett, K.D. (2015). TRIP13 is a protein-remodeling AAA+ ATPase that catalyzes MAD2 conformation switching. eLife *4*. https://doi.org/10.7554/eLife.07367.
68. Schindelin, J., Arganda-Carreras, I., Frise, E., Kaynig, V., Longair, M., Pietzsch, T., Preibisch, S., Rueden, C., Saalfeld, S., Schmid, B., et al. (2012). Fiji: an open-source platform for biological-image analysis. Nat. Methods *9*, 676–682. https://doi.org/10.1038/nmeth.2019.
69. Kaizuka, T., and Mizushima, N. (2016). Atg13 is essential for autophagy and cardiac development in mice. Mol. Cell. Biol. *36*, 585–595. https://doi.org/10.1128/MCB.01005-15.
70. Altmannova, V., Blaha, A., Astrinidis, S., Reichle, H., and Weir, J.R. (2021). InteBac: an integrated bacterial and baculovirus expression vector suite. Protein Sci. *30*, 108–114. https://doi.org/10.1002/pro.3957.
71. Weissmann, F., Petzold, G., VanderLinden, R., Huis In 't Veld, P.J., Brown, N.G., Lampert, F., Westermann, S., Stark, H., Schulman, B.A., and Peters, J.M. (2016). biGBac enables rapid gene assembly for the expression of large multisubunit protein complexes. Proc. Natl. Acad. Sci. USA *113*. E2564–E2569. https://doi.org/10.1073/pnas.1604935113.
72. Young, G., Hundt, N., Cole, D., Fineberg, A., Andrecka, J., Tyler, A., Olerinyova, A., Ansari, A., Marklund, E.G., Collier, M.P., et al. (2018). Quantitative mass imaging of single biological macromolecules. Science *360*, 423–427. https://doi.org/10.1126/science.aar5839.
73. Gürtler, A., Kunz, N., Gomolka, M., Hornhardt, S., Friedl, A.A., McDonald, K., Kohn, J.E., and Posch, A. (2013). Stain-Free technology as a normalization tool in Western blot analysis. Anal. Biochem. *433*, 105–111. https://doi.org/10.1016/j.ab.2012.10.010.
74. Holzmüller, W., and Kulozik, U. (2016). Protein quantification by means of a stain-free SDS-PAGE technology without the need for analytical standards: verification and validation of the method. J. Food Compos. Anal. *48*, 128–134. https://doi.org/10.1016/j.jfca.2016.03.003.
75. Hernandez, J.M., Stein, A., Behrmann, E., Riedel, D., Cypionka, A., Farsi, Z., Walla, P.J., Raunser, S., and Jahn, R. (2012). Membrane fusion intermediates via directional and full assembly of the SNARE complex. Science *336*, 1581–1584. https://doi.org/10.1126/science.1221976.
76. Rigaud, J.L., and Lévy, D. (2003). Reconstitution of membrane proteins into liposomes. Methods Enzymol. *372*, 65–86. https://doi.org/10.1016/S0076-6879(03)72004-7.
77. Krick, R., Busse, R.A., Scacioc, A., Stephan, M., Janshoff, A., Thumm, M., and Kühnel, K. (2012). Structural and functional characterization of the two phosphoinositide binding sites of PROPPINs, a beta-propeller protein family. Proc. Natl. Acad. Sci. USA *109*. E2042–E2049. https://doi.org/10.1073/pnas.1205128109.
78. Ploier, B., and Menon, A.K. (2016). A fluorescence-based assay of phospholipid scramblase activity. J. Vis. Exp. https://doi.org/10.3791/54635.
79. Connerth, M., Tatsuta, T., Haag, M., Klecker, T., Westermann, B., and Langer, T. (2012). Intramitochondrial transport of phosphatidic acid in

yeast by a lipid transfer protein. Science *338*, 815–818. https://doi.org/10.1126/science.1225625.

80. Miyata, N., Watanabe, Y., Tamura, Y., Endo, T., and Kuge, O. (2016). Phosphatidylserine transport by Ups2-Mdm35 in respiration-active mitochondria. J. Cell Biol. *214*, 77–88. https://doi.org/10.1083/jcb.201601082.
81. Watanabe, Y., Tamura, Y., Kawano, S., and Endo, T. (2015). Structural and mechanistic insights into phospholipid transfer by Ups1-Mdm35 in mitochondria. Nat. Commun. *6*, 7922. https://doi.org/10.1038/ncomms8922.
82. Menon, I., Huber, T., Sanyal, S., Banerjee, S., Barré, P., Canis, S., Warren, J.D., Hwa, J., Sakmar, T.P., and Menon, A.K. (2011). Opsin is a phospholipid flippase. Curr. Biol. *21*, 149–153. https://doi.org/10.1016/j.cub.2010.12.031.
83. Shevchenko, A., Tomas, H., Havlis, J., Olsen, J.V., and Mann, M. (2006). In-gel digestion for mass spectrometric characterization of proteins and proteomes. Nat. Protoc. *1*, 2856–2860. https://doi.org/10.1038/nprot.2006.468.
84. Chang, C.C., Chow, C.C., Tellier, L.C., Vattikuti, S., Purcell, S.M., and Lee, J.J. (2015). Second-generation PLINK: rising to the challenge of larger and richer datasets. GigaScience *4*, 7. https://doi.org/10.1186/s13742-015-0047-8.
85. Combe, C.W., Fischer, L., and Rappsilber, J. (2015). xiNET: cross-link network maps with residue resolution. Mol. Cell. Proteomics *14*, 1137–1147. https://doi.org/10.1074/mcp.O114.042259.
86. Kroppen, B., Teske, N., Yambire, K.F., Denkert, N., Mukherjee, I., Tarasenko, D., Jaipuria, G., Zweckstetter, M., Milosevic, I., Steinem, C., et al. (2021). Cooperativity of membrane-protein and protein-protein interactions control membrane remodeling by epsin 1 and affects clathrin-mediated endocytosis. Cell. Mol. Life Sci. *78*, 2355–2370. https://doi.org/10.1007/s00018-020-03647-z.
87. Tarasenko, D., Barbot, M., Jans, D.C., Kroppen, B., Sadowski, B., Heim, G., Möbius, W., Jakobs, S., and Meinecke, M. (2017). The MICOS component Mic60 displays a conserved membrane-bending activity that is necessary for normal cristae morphology. J. Cell Biol. *216*, 889–899. https://doi.org/10.1083/jcb.201609046.
88. Hieke, N., Löffler, A.S., Kaizuka, T., Berleth, N., Böhler, P., Drießen, S., Stuhldreier, F., Friesen, O., Assani, K., Schmitz, K., et al. (2015). Expression of a ULK1/2 binding-deficient ATG13 variant can partially restore autophagic activity in ATG13-deficient cells. Autophagy *11*, 1471–1483. https://doi.org/10.1080/15548627.2015.1068488.

STAR★METHODS

KEY RESOURCES TABLE

REAGENT or RESOURCE	SOURCE	IDENTIFIER
Antibodies		
β-Actin	Sigma-Aldrich	Cat#A5316; RRID: AB_476743
GAPDH	Abcam	Cat#ab8245; RRID: AB_2107448
Vinculin	Sigma-Aldrich	Cat#V9131; RRID: AB_477629
ATG101	CST	Cat#13492; RRID: AB_2798234
ATG13	Sigma-Aldrich	Cat#SAB4200100; RRID: AB_10602787
ATG13	CST	Cat#13468; RRID: AB_2797419
ULK1	CST	Cat# 8054; RRID: AB_11178668
FIP200	Proteintech	Cat#17250-1-AP; RRID: AB_10666428
WIPI2	Bio-Rad	Cat#MCA5780GA; RRID: AB_10845951
ATG16L	MBL	Cat#PM040; RRID: AB_1278757
ATG14	MBL	Cat#PD026; RRID: AB_1953054
ATG14 phospho S29	CST	Cat#92340; RRID: AB_2800182
ULK1 phospho S638	CST	Cat#14205; RRID: AB_2798424
ULK1 phospho S757	CST	Cat#6888; RRID: AB_10829226
HA	Biolegend	Cat#901501; RRID: AB_2565006
HA	Roche	Cat#11867423001; RRID: AB_390918
LC3B	CST	Cat#2775; RRID: AB_915950
LC3B	MBL	Cat#PM036; RRID: AB_2274121
SQSTM1/p62	PROGEN	Cat#GP62-C; RRID: AB_2687531
IRDye 680- conjugated secondary antibody	LI-COR Biosciences	Cat#926-68077; RRID: AB_10956079
IRDye 800-conjugated secondary antibody	LI-COR Biosciences	Cat#926-68076; RRID: AB_10956590
IRDye 800-conjugated secondary antibody	LI-COR Biosciences	Cat#926-68072; RRID: AB_10953628
IRDye 800-conjugated secondary antibody	LI-COR Biosciences	Cat#926-32212; RRID: AB_621847
IRDye 800-conjugated secondary antibody	LI-COR Biosciences	Cat#926-32213; RRID: AB_621848
Secondary antibodies for immunofluorescence	Invitrogen	Cat#A32731; RRID: AB_2633280
Secondary antibodies for immunofluorescence	Invitrogen	Cat#A32728; RRID:AB_2633277
Secondary antibodies for immunofluorescence	Invitrogen	Cat#A31573; RRID: AB_2536183
Bacterial and virus strains		
DH10EMBacY™	Geneva Biotech	Cat#10361012
NEB®5-alpha	New England Biolabs	Cat#C2987H
Rosetta2™	Novagen	Cat#71402
LOBSTR-BL21(DE3)-RIL	Kerafast Lcc	Cat#NC1789768
Chemicals, peptides, and recombinant proteins		
Buffers used in this study	This study	Table S3
1,2-dioleoyl-sn-glycero-3-phosphocholine (DOPC)	Avanti Polar Lipids	Cat#850375
1,2-dioleoyl-sn-glycero-3-phosphoethanolamine (DOPE)	Avanti Polar Lipids	Cat#850725
1,2-dioleoyl-sn-glycero-3-phospho-L-serine (DOPS)	Avanti Polar Lipids	Cat#840035

(*Continued on next page*)

Continued

REAGENT or RESOURCE	SOURCE	IDENTIFIER
1,2-dioleoyl-sn-glycero-3-phosphoethanolamine-N-(7-nitro-2-1,3-benzoxadiazol-4-yl) (NBD-PE)	Avanti Polar Lipids	Cat#810145
1,2-dioleoyl-sn-glycero-3-phosphoethanolamine-N-(lissamine rhodamine B sulfonyl) (RhoD-PE)	Avanti Polar Lipids	Cat#810150
1,2-dioleoyl-sn-glycero-3-phospho-(1'-myo-inositol-3'-phosphate) (PI3P)	Avanti Polar Lipids	Cat#850150
Dodecyl-β-D-maltoside (DDM)	Carl Roth	Cat#69227-93-6
n-Decyl β-maltoside (DM)	Glycon Biochemical	Cat#D322LA
Triton X-100	Merck	Cat#9036-19-5
Digitonin	Sigma Aldrich	Cat#D141
Tween 20	Roth	Cat#P1379
Amylose resin	NEB	Cat#E8021L
Pierce™ Glutathione Agarose	Thermo Fisher Scientific	Cat#16101
Pierce™ Detergent Removal Resin	Thermo Fisher Scientific	Cat#87780
Strep-Tactin Superflow Plus	Qiagen	Cat#30004
HisPur™ Cobalt Resin	Thermo Fisher Scientific	Cat#89964
Natriumhypodisulfit (Dithionite)	Sigma Aldrich	Cat#7775-14-6
Nycodenz®	Alere Technologies	Cat#AXS-1002424
Slide-A-Lyzer™ Dialysekassetten, 10 K MWCO, 12 ml	Thermo Fisher Scientific	Cat#66807
SERVA FastLoad 1 kb DNA Ladder	SERVA	Cat#39317.01
SERVA Fastload 100 bp DNA Ladder	SERVA	Cat#39316.01
SERVA DNA Stain G	SERVA	Cat#39803
All Blue Prestained Protein Standards	BioRad	Cat#1610373
Protein Dual Color Standards	BioRad	Cat#1610374
Gel Loading Dye, Purple (6X)	NEB	Cat#B7024S
BS3 (Bis(sulfosuccinimidyl)suberat)	Thermo Fisher Scientific	Cat#21580
Maltose Monohydrat	Merck	Cat#6363-53-7
L-Glutathion	Merck	Cat#70-18-8
X-TREMEGENE 9 DNA Tranfection	Merck	Cat#6365779001
Polycarbonate Membranes 0.4μm	Avanti	Cat#610007
Polycarbonate Membranes 0.1μm	Avanti	Cat#610005
10mm Filter Supports	Avanti	Cat#610014
Mini-PROTEAN® TGX Stain-Free™ Protein Gels	BioRad	Cat#4568034
4–15% Mini-PROTEAN® TGX™ Precast Protein Gels	BioRad	Cat#4561083
96-well microplate (non-binding)	Greiner Bio-one	Cat#655906
0.45um Syringe Filter	AMSTAT	Cat#C0000629
Amicon® Ultra-15 concentrator 100 kDa	Milipore	Cat#UFC910024
Amicon® Ultra-15 concentrator 30 kDa	Milipore	Cat#UFC903024
T5 exonuclease	Epicentre	Cat#T5E4111K
BSA	Roth	Cat#8076
DAPI	Roth	Cat#6335
Phusion® High-Fidelity DNA Polymerase	NEB	Cat#M0530
Q5® High-Fidelity DNA Polymerase	NEB	Cat#M0491
Taq DNA Polymerase	NEB	Cat#M0267
Taq DNA Ligase	NEB	Cat#M0208
BamHI	NEB	Cat#R0136S

(*Continued on next page*)

Continued

REAGENT or RESOURCE	SOURCE	IDENTIFIER
HindIII	NEB	Cat#R0104S
Proteinase K	Sigma Alrich	Cat#39450-01-6
Benzonase®	Merck	Cat#E1014
Dpn1	NEB	Cat#R0176S
Critical commercial assays		
QIAprep Spin Miniprep Kit	Qiagen	Cat#27106
Plasmid Mediprep Kit	Invitrogen	Cat#K210015
QIAquick PCR purification Kit	Qiagen	Cat#28106
HiPPR Detergent Removal Spin Column Kit	Thermo Fisher Scientific	Cat#PI88305
Atto 647N Protein Labeling Kit	Jena Bioscience	Cat#FP-201-647N
Alexa Fluor™ 488 Protein Labeling Kit	Invitrogen	Cat#A10235
Zeba™ Spin-Entsalzungssäulen, 7 K MWCO, 0,5 ml	Thermo Fisher Scientific	Cat#89882
LB medium	BioChemica	Cat#23143289
LB-agar	Roth	Cat#X969.2
ESF 921 medium	Expression Systems	Cat#96-001-01
Sf-900 medium	Gibco	Cat#12658-019
Bafilomycin A_1	Sigma-Aldrich	Cat#B1793
DPBS	Gibco	Cat#14190-094
EBSS	Gibco	Cat#24010-043
GlutaMAX™-I	Gibco	Cat#36600-021
FuGENE® 6	Promega	Cat#E2691
Polybrene	Sigma Alrich	Cat#H9268-106; Cat#sc-134220
puromycin	InvivoGen	Cat#ant-pr-1
blasticidin	InvivoGen	Cat#ant-bl-05
PhosSTOP	Roche	Cat#04906837001
Deposited data		
Uncropped Western blot and gels images, raw microscopy images	This paper, Mendeley data	https://doi.org/10.17632/dyy8xfvpkf.1
Experimental models: Cell lines		
Sf9 insect cells	Invitrogen	Cat#10503433
High Five insect cells	Invitrogen	Cat#10747474
Oligonucleotides		
Oligonucleotides used in this study	This study	Table S4
Recombinant DNA		
pLIB-6x-His-MBP-ATG9	This study	N/A
pLIB-ATG2-StrepII	This study	N/A
pLIB-6xHis-GFP-WIPI4	This study	N/A
pLIB-GST-WIPI4	This study	N/A
pLIB-ATG101-StrepII	This study	N/A
pBIG-6x-His-MBP-ATG13^{HORMA}-ATG101	This study	N/A
pBIG-GST-ATG13^{HORMA}-ATG101	This study	N/A
pLIB-6x-His-MBP-FIP200	This study	N/A
pLIB-6x-His-MBP-ATG13	This study	N/A
pLIB-6x-His-MBP-BECN1	This study	N/A
pLIB-GST-ULK1	This study	N/A
pLIB-6xHis-mCherry-ATG14	This study	N/A
pLIB-6x-His-MBP-ATG13^{HORMA}	This study	N/A

(*Continued on next page*)

Continued

REAGENT or RESOURCE	SOURCE	IDENTIFIER
pLIB-GST- ATG13^{HORMA}	This study	N/A
pLIB-GST- ATG13$^{HORMA_\Delta SB1}$	This study	N/A
pLIB-6x-His-MBP- ATG13$^{HORMA_\Delta SB1}$	This study	N/A
pLIB-6x-His-MBP- ATG13$^{HORMA_\Delta SB2}$	This study	N/A
pLIB-6x-His-MBP-ATG101	This study	N/A
pLIB-GST-ATG101	This study	N/A
pLIB-GST-ATG9^{C}	This study	N/A
pLIB-GST-ATG9$^{C,\ P833A,\ P834A}$	This study	N/A
pLIB-6xHis-mCherry-ATG9^{N}	This study	N/A
pLIB-GST-ATG9^{N}	This study	N/A
pLIB-6x-His-MBP-ATG9^{N}	This study	N/A
pLIB-6xHis-GFP-ATG14	This study	N/A
pLIB-BECN1	This study	N/A
pLIB-6x-His-MBP-ATG9^{core}	This study	N/A
pLIB-6x-His-MBP-ATG9^{core+C}	This study	N/A
pLIB-6x-His-MBP-ATG9^{N+core}	This study	N/A
pBIG-GST-ATG13^{HORMA}-6xHis-mCherry-ATG9^{N}	This study	N/A
pLIB-6x-His-MBP- ATG13$^{HORMA_\Delta N}$	This study	N/A
pLIB-6x-His-MBP- ATG13^{LL}	This study	N/A
Software and algorithms		
JalView	Barton Group (University of Dundee)	2.11.1.5
PyMol	Schrödinger, LLC	2.5.2
AlphaFold 2	DeepMind (Alphabet Inc.)	2
Adobe Creative Cloud	Adobe Inc.	5.8.0.592
Graphpad PRISM	GraphPad Software Inc.	9.0.0
ImageJ	NIH, USA	1.53t
Image Studio Lite	LI-COR Biosciences	5.2
ChimeraX 1.4	UCSF	1.4
Snapgene	GSL Biotech	5.3.2
Fiji	Schindelin et al.[68]	1.53
Microsoft® Office	Microsoft Corporation	16.64
Others		
MBPTrap™ HP (1 ml; 5 ml)	Cytiva	Cat#29048641; Cat#28918778
HiTrap TALON crude (1 ml; 5ml)	Cytiva	Cat#29048565; Cat#28953766
GSTrap™ HP (1 ml; 5 ml)	Cytiva	Cat#17528101; Cat#17528201
StrepTrap HP (5ml)	Cytiva	Cat#28907546
HiLoad 16/600 Superdex 75 pg	Cytiva	Cat#28989333
HiLoad 16/600 Superdex 200 pg	Cytiva	Cat#28989335
HiLoad 16/600 Superose 6 pg	Cytiva	Cat#29323952
Superdex 75 Increase 10/300 GL	Cytiva	Cat#29148721
Superdex 200 Increase 5/150 GL	Cytiva	Cat#28990945
Superose 6 Increase 10/300 GL	Cytiva	Cat#29091596
Superose 6 Increase 5/150 GL	Cytiva	Cat#29091597
RESOURCE Q, 6 ml	Cytiva	Cat#17117901
ProLong Glass Antifade Mountant	Thermo Fisher Scientific	Cat#P36980

RESOURCE AVAILABILITY

Lead contact

Further information and requests for reagents should be directed to and will be fulfilled by the lead contact, Alex Faesen (alex.faesen@mpinat.mpg.de).

Materials availability

Plasmids generated in this study are available from the lead contact. They might require a completed materials transfer agreement if there is potential for commercial application.

Data and code availability

- All data generated or analysed during this study are included in this published article (and its supplemental information files). Original SDS-PAGE gels, Western blot data and microscopy images used in this paper have been deposited at Mendeley Data and are publicly available as of the date of publication. The DOI is listed in the key resources table.
- This paper does not report original code.
- Any additional information required to reanalyze the data reported in this paper is available from the lead contact upon request.

EXPERIMENTAL MODEL AND STUDY PARTICIPANT DETAILS

E. coli strains and media

E. coli (DH5α and DH10 α) were grown in Luria-Bertani broth (LB) medium.

Insect cells and media

Insect cells (Sf9 and High Five cells; Invitrogen) were grown in Sf900 II medium (GIBCO).

Cell lines and cell culture

Wild-type and *atg13* KO MEFs were provided by Noboru Mizushima (University of Tokyo, Japan) and have previously been described and authenticated.[27,69] HCT116 (male) ATG9A-HA KI cells and HCT116 ATG9A-HA KI ATG9 KO or ATG101 KO or ATG13 KO cells were provided by Joshua L. Andersen (Brigham Young University, Utah, US) and have previously been described and authenticated.[26] Wild-type MEFs, *atg13* KO MEFs, *atg101* KO MEFs and corresponding transfectants generated in this study were cultured in high-glucose (4,5 g/L) DMEM (Gibco, #41965-039) supplemented with 10% FCS (Sigma-Aldrich, #F0804, LOT BCCB7649 and #F9665, LOT 0001655429), 100 U/ml penicillin and 100 μg/ml streptomycin (Gibco, #15140-122) at 37 °C and 5% CO_2 humidified atmosphere. HCT-116 cells were cultured in McCoy's 5A (1X) + GlutaMAX™-I (Modified Medium) (Gibco, #36600-021) supplemented with 10% FCS, 100 U/ml penicillin and 100 μg/ml streptomycin at 37 °C and 5% CO_2 humidified atmosphere.

METHOD DETAILS

Reagents & antibodies

All phospholipids used in this study were purchased from Avanti Polar Lipids. Bafilomycin A_1 (#B1793) was purchased from Sigma-Aldrich (St. Louis, MO, USA). Additionally, the following reagents were used: Primary antibodies against β-Actin (WB: 1:20 000, clone AC-74, Sigma-Aldrich, #A5316), GAPDH (WB: 1:5000, abcam, #ab8245), Vinculin (WB: 1:1000, Sigma-Aldrich, #V9131), ATG101 (WB: 1:1000, CST, #13492), ATG13 (WB: 1:1000, Sigma-Aldrich, SAB4200100; IF: 1:100, CST #13468), ULK1 (WB: 1:1000, clone D8H5, CST, #8054), FIP200 (WB: 1:1000; IF: 1:500, Proteintech, #17250-1-AP), WIPI2 (IF: 1:200, Bio-Rad, #MCA5780GA), ATG16L (IF: 1:200, MBL, #PM040) ATG14 (WB: 1:1000, MBL, #PD026), ATG14 phospho S29 (WB: 1:1000; IF: 1:400, CST, #92340), ULK1 phospho S638 (WB: 1:1000, CST, #14205; corresponds to murine S637), ULK1 phospho S757 (WB: 1:1000, CST, #6888; corresponds to human S758), HA (WB and IF: 1:1000, Biolegend, #901501 and Roche, #11867423001 (only for WB)), LC3B (WB: 1:1000, CST, #2775; IF: 1:500, MBL, #PM036) and SQSTM1/p62 (WB: 1:1000, PROGEN, #GP62-C) were used. IRDye 680- or IRDye 800-conjugated secondary antibodies (#926-68077, #926-68076, #926-68072, #926-32212, #926-32213) were purchased from LI-COR Biosciences. Secondary antibodies for immunofluorescence (#A32731, #A32728, #A31573) were purchased from Invitrogen (Waltham, MA, USA).

Expression and purification of proteins

ATG9A and its transmembrane containing constructs

ATG9A with a tandem N-terminal 6xHis-MBP tag was expressed in High Five™ (Hi5) cells using the biGBac and InteBac expression system.[70,71] Cell pellet was resuspended in lysis buffer A. Cells were lysed on ice for at least 1 h by stir-mixing. The lysate was then diluted 3 times with DDM-free buffer A and stir-mixed for another 30 min before clarifying by centrifugation at 20,000 × *g* for 30 min. The protein was purified from the lysate by affinity chromatography using an MBP trap column (Cytiva) with buffer B as binding buffer

and buffer B supplemented with 20 mM maltose as elution buffer. The affinity tags were cleaved by incubation with PreScission protease (ratio 1:1000 – PreScission protease: protein) for at least 5 hours at 4 °C after affinity chromatography (if required), followed by size exclusion chromatography (SEC) using a Superose 6 column (Cytiva) pre-equilibrated with buffer B. The purified protein was concentrated, flash-frozen in liquid nitrogen, and stored at - 80 °C.

ATG9-13-101

To purify a complex of human ATG9A, ATG13, ATG101, each protein with a tandem N-terminal 6xHis-MBP tag was co-expressed in Hi5 cells and purified with the same protocol used for ATG9A.

ATG9^{N}

ATG9^{N} was produced as GST, 6xHis-mCherry, or 6xHis-MBP fusion constructs from Hi5 cells, as described previously. Harvested cells were resuspended in lysis buffer C. The resuspended cells were lysed by stirring for 1 h in the presence of DNase I (20 μg/ml) and cleared by centrifugation at 15,000 × *g* for 30 minutes. The clarified lysate was purified by affinity chromatography using MBPTrap HP columns, GSTrap HP column, or HisTrap excel column (Cytiva) with buffer D as binding buffer. The proteins were eluted using a 0-300 mM imidazole gradient, 10 mM reduced glutathione, or 20 mM maltose depending on the column used. The eluted protein was concentrated in a Amicon-Ultra-15 Centrifugal Filter 50 kDa MWCO (Millipore). Concentrated protein was then loaded onto a Superdex 200 column or a Superose 6 column (Cytiva) pre-equilibrated in buffer D. The peak fractions corresponding to ATG9^{N} were collected and again concentrated in a Amicon-Ultra-15 Centrifugal Filter 50 kDa MWCO to at least 1 mg/ml before being flash-frozen in liquid nitrogen and stored at - 80 °C.

ATG9^{N}-ATG13^{HORMA}

The ATG9^{N}-ATG13^{HORMA} complex was produced as N-terminal GST-ATG13^{HORMA} and 6xHis-mCherry-ATG9^{N} fusion constructs from Hi5 cells using the biGBac expression system. Harvested cells were resuspended in lysis buffer C. The resuspended cells were lysed by stirring for 4 h in the presence of DNase I (20 μg/ml) before clearance by centrifugation at 15,000 × *g* for 30 min. The cleared lysate was filtered and passed over a GSTrap column (Cytiva) before extensive washing with buffer D. The complex was then eluted in buffer D supplemented with 20 mM reduced glutathione or 100 mM imidazole depending on the column used. The eluted protein was concentrated in a Amicon-Ultra-15 Centrifugal Filter 50 kDa MWCO (Millipore) and then loaded onto a Superose 6 column (Cytiva), pre-equilibrated in buffer D. The peak fractions corresponding to ATG9^{N}- ATG13 ^{HORMA} were collected and again concentrated in Amicon-Ultra-15 Centrifugal Filter 50 kDa MWCO to at least 1 mg/ml before being flash-frozen in liquid nitrogen and stored at - 80 °C.

ATG9^{C}

ATG9^{C} and its mutant were produced as N-terminal GST fusion constructs from *E. coli* expression system (Rosetta and Lobster expression cell lines). Cells were washed and resuspended in lysis buffer E and lysed by stir-mixing for 1 h before clearance by centrifugation at 15,000 × *g* for 30 minutes. The cleared lysate was passed over GSTrap column (Cytiva) before extensively washed with buffer D. ATG9^{C} was then eluted in buffer D, supplemented with 20 mM reduced glutathione. Eluted protein was concentrated in a Amicon-Ultra-15 Centrifugal Filter 10 kDa MWCO (Millipore). Concentrated protein was then loaded onto a Superdex 200 column (Cytiva), pre-equilibrated in buffer F. The peak fractions corresponding to ATG9^{C} were collected and again concentrated in a 10 kDa MWCO concentrator to at least 1 mg/ml before being flash-frozen in liquid nitrogen and stored at - 80 °C.

ATG13

ATG13^{HORMA} and its mutants were produced as N-terminal GST or 6xHis-MBP fusion constructs from Hi5 cells using the biGBac expression system. Cells were washed and resuspended in lysis buffer C. The resuspended cells were lysed by stirring for 3 to 4 h in the presence of DNase I (20 μg/ml) before clearance at 15,000 × *g* for 30 minutes. Cleared lysate was filtered and passed over GSTrap or MBPTrap column (Cytiva) before extensive washing with buffer D. ATG13 was then eluted in buffer D, supplemented with 20 mM reduced glutathione or 20 mM maltose depending on the column used. Eluted protein was concentrated in a Amicon-Ultra-15 Centrifugal Filter 50 kDa MWCO (Millipore). Concentrated protein was then loaded onto a Superdex 200 column or a Superose 6 column, pre-equilibrated in buffer D. Peak fractions corresponding to ATG13^{HORMA} were collected and again concentrated in a 50 kDa MWCO concentrator (Millipore) to at least 1 mg/ml before being flash-frozen in liquid nitrogen and stored at - 80 °C.

Full-length ATG13 (N-terminal 6xHis-MBP-tagged) was expressed in Hi5 cells. Cell pellets were resuspended in 50 ml lysis buffer F and sonicated for 5 min (5 s on and 10 s off at an amplitude of 25 %). The lysate was then stir-mixed after addition of 0.2 % DDM, 20 μg/ml DNase I (20 μg/ml), 5 mM $MgCl_2$ for 30 min, after which it was diluted to 250 ml with buffer G. Clarification of lysate was done by centrifugation at 10,000 rpm for 30 min at 4 °C and supernatant loaded on an MBPTrap column (Cytiva). The protein was purified from the lysate by affinity chromatography using an MBP trap column (Cytiva) with buffer G as binding buffer and buffer G supplemented with 20 mM maltose as elution buffer. Following affinity purification, peak fractions were pooled, concentrated with Amicon-Ultra-15 Centrifugal Filter 50 kDa MWCO (Millipore), measured for amount of protein and loaded on a Superose 6 16/600 column, equilibrated with buffer G. For cleaving the N-terminal 6xHis-MBP tag, the protein was incubated with PreScission protease (ratio 1:1000 – PreScission protease: protein) overnight at 4 °C, and purified by SEC using buffer G. Fractions corresponding to ATG13 were concentrated and stored by flash-freezing at - 80 °C.

ATG101

ATG101 was produced as N-terminal GST, 6xHis-MBP, or C-terminal Strep fusion constructs from Hi5 cells using the biGBac expression system. Cell pellets were washed and resuspended in lysis buffer C. The resuspended cells were lysed by stirring for 1 h in the presence of DNase I (20 μg/ml) and cleared by centrifugation at 15,000 × *g* for 25 minutes. The cleared lysate was filtered

and passed over GSTrap, MBPTrap, or StrepTrap column (Cytiva) before extensive washing with buffer D. ATG101 was then eluted in buffer D, supplemented with 20 mM reduced glutathione, 20 mM maltose, or 5 mM desthiobiotin (Sigma) depending on the column used. Eluted protein was concentrated in a Amicon-Ultra-15 Centrifugal Filter 30 kDa or 10 kDa MWCO (Millipore). Depending on experiments, affinity tag was cleaved by incubation with PreScission Protease (ratio 1:1000 – PreScission protease: protein) overnight at 4 °C. Concentrated protein was then loaded onto a Superdex 200 column or Superdex 75 column, pre-equilibrated in buffer D. In the case of the cut protein, a 1 ml GST Trap or a HisTrap excel column (Cytiva) was connected in series after the Superdex column to trap the tag, un-cut ATG101, and tagged PreScission Protease. The peak fractions corresponding to ATG101 were collected and again concentrated in a 30 or 10 kDa MWCO concentrator to at least 1 mg/ml before being flash-frozen in liquid nitrogen and stored at - 80 °C.

ATG2A

Human ATG2A with a C-terminal StrepII tag expressed in Hi5 cells were purified similarly by affinity chromatography using Strep trap columns (Cytiva) with buffer A as lysis buffer, buffer H as binding buffer, and buffer H supplemented with 5 mM desthiobiotin as elution buffer. The protein was finally purified by SEC using Superose 6 column (Cytiva), pre-equilibrated with buffer H. The purified protein was concentrated, flash-frozen in liquid nitrogen and stored at - 80 °C. For lipid transfer assay, DDM was subsequently removed by three successive incubations with Pierce detergent removal resin (Thermo Fisher Scientific), pre-equilibrated with buffer D. Incubation in the detergent removal resin was performed at room temperature for 15 min each.

ULK1

ULK1 with N-terminal GST tag was expressed in Hi5 cells. Harvested cells were lysed by stir-mixing in buffer I for 1 h on ice. The lysate was then diluted 3 times with DDM-free buffer I and mixed gently for another 30 min. The protein was purified from the lysate by affinity chromatography using GST trap column (Cytiva) using buffer J as binding buffer and buffer J supplement with 10 mM reduced glutathione as elution buffer. The protein was subjected to SEC with Superose 6 column (Cytiva), pre-equilibrated with buffer J. The purified protein was concentrated, flash-frozen in liquid nitrogen and stored at - 80 °C.

FIP200

FIP200 with a tandem N-terminal 6xHis-MBP tag expressed in Hi5 cells was purified similarly by affinity chromatography using MBP trap columns (Cytiva) with buffer K as lysis buffer, buffer L as binding buffer, and buffer L supplemented with 20 mM maltose as elution buffer. The proteins were finally purified by size exclusion chromatography using a Superose 6 column (Cytiva), pre-equilibrated with buffer L. The purified proteins were concentrated, flash-frozen in liquid nitrogen, and stored at - 80°C.

ATG14-BECN1

The ATG14 and BECN1 complex was co-expressed as an N-terminal 6xHis-GFP-ATG14 construct and BECN1 from Hi5 insect cells using the biGBac expression system. Cell pellets were washed and resuspended in lysis buffer M. Resuspended cells were lysed by stirring for 2 h in the presence of DNase I (20 μg/ml) before clearance by centrifugation at 15,000 x *g* at 4 °C for 30 minutes. Cleared lysate was filtered and passed over a HisTrap™ excel 5 ml column before extensive washing with binding buffer N. ATG14-BECN1 complex was then eluted by a 0-300 mM linear gradient of imidazole. The complex eluted around 100 mM imidazole was then incubated overnight at 4 °C in the presence of PreScission protease (ratio 1:1000 – PreScission protease: protein) and subsequently loaded onto an anion exchange column to separate the tag using a salt gradient (5 to 1000 mM NaCl). The complex eluted at around 400 mM NaCl. Eluted product was concentrated using an Amicon-Ultra-15 Centrifugal Filter 100 kDa MWCO (Millipore) and loaded on a Superdex 200 column pre-equilibrated in buffer O. Peak fractions corresponding to ATG14-BECN1 were collected and again concentrated to at least 1 mg/ml before being flash-frozen in liquid nitrogen and stored at - 80 °C.

WIPI4

WIPI4 with different tag variants (N-terminal GST tag, tandem N-terminal 6xHis-GFP tag or tandem N-terminal 6xHis-mCherry tag) were expressed in Hi5 cells and purified similarly by affinity chromatography using an appropriate affinity column (GSTrap or HisTrap). Cell pellets were lysed by sonication in DDM-free buffer A. Clarified lysate was applied to appropriate affinity chromatography columns using DDM-free buffer A as binding buffer and eluted by either 0 to 300 mM imidazole gradient or 10 mM reduced glutathione depending on the column used. The tag was cleaved if required as described above and the proteins were finally purified by size exclusion chromatography using Superdex S200 column (Cytiva) pre-equilibrated with buffer D. The purified protein was concentrated, flash-frozen in liquid nitrogen and stored at - 80 °C.

Analytical size-exclusion chromatography

Analytical SEC analysis was performed using the indicated column in appropriate SEC buffer on an ÄKTA Pure system. All samples were eluted under isocratic conditions at 4 °C in SEC buffer at a flow rate of 0.5 ml/min. Elution of proteins was monitored by absorption of UV light at 280 nm. Fractions (0.5 ml) were collected and analyzed by SDS-PAGE. To detect the formation of a complex, proteins were mixed at the indicated concentrations in 250 μl, incubated on ice for at least 1 h and then subjected to SEC.

GST, MBP and Strep pulldown assays

GST, MBP and Strep pulldown experiments were performed using GSH Sepharose beads, MBP beads (Amylose resin) (NEB), or StrepTactin Superlow Plus (Qiagen) beads pre-equilibrated in pulldown buffer (50 mM HEPES (pH 8), 150 mM NaCl, 0.5 mM TCEP). The pulldown buffer was supplemented with 0.03% DDM whenever ATG9 was present or 1 % DDM and 1 mM PMSF if it involved pure lysate from cells. Pulldowns that required incubation of the bait and prey for less than 1 h, were performed by

pre-incubating the bait with 30 μl of beads before the prey was added. In case of incubation longer then 1 h, the prey and bait were pre-incubated and then added to the beads for 10 minutes. Beads were spun down at 500 × *g* for 1 min. The supernatant was removed, and beads were washed twice with 500 μl buffer. The supernatant was removed completely, samples boiled in 5 μl of 4x Laemmli sample loading buffer and run on a 12 % SDS–PAGE gel. Bands were visualized with Coomassie brilliant blue staining. For information regarding concentration, temperature, and variations, see figure legends.

Crosslinking with glutaraldehyde

The ^{MBP}ATG13^{HORMA}-101 complex, amphipol-reconstituted ^{MBP}ATG9, and amphipol-reconstituted ^{MBP}ATG9-^{MBP}13^{HORMA}-101 complex, were crosslinked by incubating for 1 hour at 4 °C with 0.01% glutaraldehyde. The crosslinked samples were then quenched by adding 50 mM Tris pH8 and incubating for 15 min. Quenched samples were used for mass photometry measurements.

Anion exchange chromatography

Purified ATG13 and ATG101 were subjected to anion-exchange (AE) chromatography using 750 μg of protein in 500 μl low salt buffer (containing 25 mM Hepes (pH 8), 50mM NaCl, 0.5 mM TCEP) on a 1 ml Hi-Trap Q column (Cytiva). Bound proteins were eluted using a 50-350 mM NaCl gradient over 20 column volumes. Fractions were analysed by 12% SDS-PAGE gel and pull-downs.

Mass photometry

Mass photometry (MP) is a technique to measure molecular weight of biomolecules in solutions.[72] Membrane proteins were reconstituted with amphipols before MP measurements to avoid the noisy background caused by detergent micelles. For amphipol reconstitution, purified ^{MBP}ATG9 or ^{MBP}ATG9-^{MBP}ATG13^{HORMA}-ATG101 complex in buffer containing detergent were incubated with amphipol PMAL-C8 in a protein:amphipol ratio of 1:3 (w/w) for at least 2 hours at 4 °C. Detergent and unbound PMAL-C8 were subsequently removed by SEC using a Superpose 6 column, pre-equilibrated with buffer (50 mM HEPES (pH 8), 150 mM NaCl, 0.5 mM TCEP) . The ^{MBP}ATG13^{HORMA}-ATG101 complex, amphipol-reconstituted ^{MBP}ATG9, and amphipol-reconstituted ^{MBP}ATG9-^{MBP}ATG13^{HORMA}-ATG101 complex were then crosslinked by incubating for 1 hour at 4 °C with 0,01% glutaraldehyde. The crosslinked samples were then quenched by adding 50vmM Tris (pH 8) and incubating for 15 min. Quenched samples were used for MP measurements. MP measurements were performed using a OneMP mass photometer (Refeyn Ltd, Oxford, UK). Data was acquired using the AcquireMP software (Refeyn Ltd. v2.3). For the measurement, a drop of immersion oil was first applied on top of the microscope objective. Then, a clean coverslip was placed on the microscope stage. Clean silicon gasket wells to hold the samples were then placed on the cover slip. To find focus, 20 μl of filtered and degassed buffer (50 mM HEPES (pH 8), 150 mM NaCl, 0.5 mM TCEP) was pipetted into one gasket well. The focal point was then identified and locked using the autofocus function. Each sample at an approximate concentration of 20 nM was pipetted into a gasket well, and data were acquired with an acquisition time varying between 60 s and 120 s. The timing was adjusted to get a good number of landing events while avoiding saturation. DiscoverMP software (Refeyn Ltd. v2.3) was used to analyze the data.

Stain-free protein quantification

Stain-Free (SF) is a method of protein visualization and quantification which enables detection of protein bands in gels without using colorimetric or fluorescent stains.[73,74] SF gels contain a trihalo compound within the gel matrix which reacts with tryptophan residues using an ultraviolet light-induced reaction to produce fluorescent light. The fluorescence allows visualization of proteins in the gel without additional staining and de-staining steps. In this study, to quantify the relative amount of each protein in a complex, purified protein complexes in increasing amount (5 μg, 10 μg, 15 μg, 20 μg) were loaded on 12 % Mini-PROTEAN® TGX Stain-Free™ Protein Gels (Bio-Rad Laboratories) and separated by electrophoresis. After electrophoresis protein bands were visualized by placing the gel on the UV transilluminator Gel Doc™ EZ imager (Bio-Rad Laboratories). Intensities of protein bands were then normalized against the number of tryptophan residue in each protein. A linear fit of the band intensities against the amount of protein was fitted to verify that the intensity proportionally increases with the increase in protein loaded (5 μg, 10 μg, 15 μg, 20 μg).

Preparation of protein-free liposomes

Large Unilamellar Vesicles (LUVs) were prepared by reversed-phase evaporation as described previously.[75] Briefly, lipids were dissolved in chloroform and mixed at a desired molar ratio (donor LUVs: 46% DOPC, 25% DOPE, 20% DOPS, 2% NBD-PE, and 2% Rh-PE, 5% PI3P; acceptor LUVs: 50% DOPC, 25% DOPE, and 25% DOPS). Chloroform was subsequently removed using a rotary evaporator to allow lipid film formation. The lipid film was then dissolved in 1 ml diethyl ether, followed by 300 μl of buffer (50 mM HEPES (pH 8), 150 mM NaCl, 0.5 mM TCEP). The sample was then sonicated for 1 min in a bath sonicator at 4 °C to create emulsion. Diethyl ether was initially removed at 500 mbar for 10 min, and 700 μl of buffer F was added. The remaining diethyl ether was removed by lowering the pressure stepwise to 100 mbar until diethyl ether was completely removed. The resulting lipid suspension was extruded 11 times through a 0.4-μm polycarbonate filter and then 21 times through a 0.1-μm polycarbonate filter (Mini extruder kit, Avanti Polar Lipids).

Reconstitution of proteins into liposomes

For proteo-liposome reconstitution, the protein-free liposome was destabilized by the addition of the detergent n-Decyl-Beta-Maltoside (DM) at the concentration described by the R-value[76]:

$$R = \frac{D_{total} - D_{CMC}}{[lipid]}$$

where D_{total} is total detergent concentration, D_{CMC} is critical micellar concentration of the detergent, and [*lipid*]: total lipid concentration. To reconstitute ATG9, DM (R-value of 1.5) was added to protein-free liposomes, followed by protein at a protein:lipid ratio of 1:2000 or 1:500 depending on the experiments. The solution was incubated for 1 h at room temperature and DM was subsequently removed by three successive incubations with Pierce detergent removal resin (Thermo Fisher Scientific), pre-equilibrated with buffer (50 mM HEPES (pH 8), 150 mM NaCl, 0.5 mM TCEP). Incubation in the detergent removal resin was performed at room temperature for 15 min each.

Flotation of reconstituted liposome

Flotation assay was performed as described previously[77] to verify proper reconstitution of ATG9 into protein-free liposome. Briefly, 50 μl of ATG9 proteo-liposomes were mixed with 50 μl 80% (w/v) Nycodenz (Alere Technologies) prepared in buffer (50 mM HEPES (pH 8), 150 mM NaCl, 0.5 mM TCEP). The mixture was subsequently overlaid with 40 μl of 30% Nycodenz, 40 μl 15% Nycodenz and 40 μl of buffer (50 mM HEPES (pH 8), 150 mM NaCl, 0.5 mM TCEP), respectively. The density gradient was centrifuged at 50,000 rpm in a S55-S swinging bucket rotor (Thermo Fisher Scientific) for 1 h at 4 °C. Six equal fractions were collected from the top of the gradient and analyzed by SDS-PAGE.

Protease protection assay

The orientation of MBP-ATG9 in the proteo-liposomes was determined by assessing the accessibility of the N-terminal HRV 3C-cleavage site (positioned between the MBP tag and ATG9) to PreScission protease. Proteo-liposomes were incubated with 10 μM PreScission protease at 4 °C for 20 min, 40 min, or overnight. In the control, 1% DDM was added to the proteo-liposomes and precision protease mix. The reactions were stopped by addition of SDS loading buffer and samples were analyzed by SDS-PAGE. Gels were quantified using Fiji (ImageJ).[68]

Leakiness control

To test for leaking reconstituted vesicles, a protocol similar to the scramblase assay was used.[78] PLs were reconstituted as described previously, with the exception that the reconstitution buffer was supplemented with 100 μM NBD-glucose and fluorescent lipids were not incorporated into the liposome templates. Liposome templates underwent the same procedure as controls. After reconstitution, NBD-glucose was captured inside the liposome templates and PLs, while extravesicular NBD-glucose was removed by dialysis following the manufacturer's protocol for Slide-A-Lyzer™ Dialysis cassettes (Thermo Fisher Scientific). 50 μM of liposomes or ATG9 PLs containing NBD-glucose were prepared in 200 μl buffer (50 mM HEPES (pH 8), 150 mM NaCl, 0.5 mM TCEP) in a 96-well microplate (Greiner bio-one). The microplate was placed in a Synergy Neo 2 Multi-Mode Reader (BioTek) and NBD fluorescence intensity (excitation, 485 nm; emission, 528 nm) was monitored. After initial signal stabilization, the solution was supplemented with 50 mM sodium dithionite and further supplemented with 50 mM dithionite and Triton X-100 0.5 % (v/v) after 10 to 15 min of incubation.

Lipid transfer assay

To monitor protein mediated lipid transfer between liposomes, we performed FRET-based dequenching assays as described previously.[79–81] In brief, a mixture of donor liposomes containing fluorescent lipids NBD-PE and Rh-PE (46 % DOPC, 25 % DOPE, 20 % DOPS, 2 % NBD-PE, and 2 % Rh-PE, 5% PI3P), and acceptor liposomes without fluorescent lipids (50% DOPC, 25% DOPE, and 25% DOPS) were prepared. In the donor liposome, NBD-PE fluorescence is quenched by Rh-PE. Upon lipid exchange between liposomes, the NBD will be dequenched and the fluorescence will increase. In our experiments, 25 μM lipid concentration of donor liposomes and acceptor liposomes in the presence or absence of the indicated proteins except ATG2 was prepared in 200 μl buffer (50 mM HEPES (pH 8), 150 mM NaCl, 0.5 mM TCEP) in a 96-well microplate (Greiner bio-one). In the sample containing ATG9, the protein was reconstituted into both donor and acceptor liposomes. The microplate was placed in a Synergy Neo 2 Multi-Mode Reader (BioTek) and gently shaken for 30 min at 25 °C. Subsequently, ATG2 was added at the desired concentrations to start the reaction and NBD fluorescence intensity (excitation, 485 nm; emission, 528 nm) was monitored for 2 or 3 hours. A lag time was expected between samples due to preparation of the mixtures. After the indicated time, Triton X-100 was added to the reaction mixture at 0.5 % (v/v) final concentration to solubilize all lipids and therefore maximize NBD fluorescence signal. The activities shown in one figure were simultaneously measured. All proteins used in lipid transfer were un-tagged except ATG2 with C-terminal StrepII tag. All data were normalized as a percentage of total NBD fluorescence after Triton-X100 addition. Transfer rate (k_{obs}) was obtained by fitting the data to a one-phase exponential association equation using GraphPad Prism.

Scramblase assay

The scramblase assay of ATG9 was performed as previously reported.[78,82] In brief, proteo-liposomes or protein-free liposomes containing a trace amount of NBD-PE distributed equally between both leaflets are supplemented with dithionite. Dithionite irreversibly quenches NBD fluorophore on the outer leaflet, but not the inner leaflet. Hence, dithionite addition leads to a 50 % decrease of fluorescence for protein free liposomes and a greater reduction for scramblase-containing proteo-liposomes due to the rapid exchange of lipids between leaflets induced by the scramblase protein. In our experiments, 50 μM of protein-free liposome/ATG9 proteo-liposome-containing NBD-lipids were prepared in 200 μl buffer (50 mM HEPES (pH 8), 150 mM NaCl, 0.5 mM TCEP) in a 96-well microplate (Greiner bio-one). The microplate was placed in a Synergy Neo 2 Multi-Mode Reader (BioTek) and NBD fluorescence intensity (excitation, 485 nm; emission, 528 nm) was monitored. After initial signal stabilization, the solution was supplemented with 50 mM sodium dithionite and further supplemented with Triton X-100 0.5 % (v/v) and 50 mM sodium dithionite after about 600 s of incubation. In the experiment with the ATG13^{HORMA}-ATG101 complex, indicated amount of ATG13^{HORMA}-ATG101 complex were pre-incubated with protein-free liposome/ATG9 proteo-liposome for 30 min at 25 °C.

CXL-MS analysis

To cross-link the ATG9-13^{HORMA}-101 complex, 3 μM of the complex was incubated with the indicated amount of BS3 (Thermo Scientific), incubated at 4 °C for 60 min and subsequently quenched by addition of 50 mM Tris pH 8 (final concentration) for 15 min. Proteins were then separated by SDS-PAGE using a 4–12 % gradient gel (BioRad). The cross-linked complex was cut out of the gel. Excised gel pieces were then subjected to in-gel tryptic digest.[83] Samples were reduced with 10 mM dithiotreitol and alkylated with 55 mM iodacetamide and subsequently digested with trypsin (sequencing grade, Promega) at 37 °C for 18 h. Extracted peptides were dried in a SpeedVac Concentrator and dissolved in loading buffer composed of 4 % acetonitrile and 0.05 % TFA. Samples were subjected to liquid chromatography mass spectrometry (LC-MS) on a QExactive HF-X (Thermo Scientific). Peptides were loaded onto a Dionex UltiMate 3000 UHPLC+ focused system (Thermo Scientific) equipped with an analytical column (75 μm x 300 mm, ReproSil-Pur 120 C18-AQ, 1.9 μm, Dr. Maisch GmbH, packed in house). Separation by reverse-phase chromatography was done on a 60 min multi-step gradient with a flow rate of 0.3-0.4 μl min^{-1}. MS1 spectra were recorded in profile mode with a resolution of 120 k, maximal injection time was set to 50 ms and AGC target to 1e^6 to acquire a full MS scan between 380 and 1580 m/z. The top 30 abundant precursor ions (charge state 3-8) were triggered for HCD fragmentation (30 % NCE). MS2 spectra were recorded in profile mode with a resolution of 30 k; maximal injection time was set to 128 ms, AGC target to 2e^5, isolation window to 1.4 m/z and dynamic exclusion was set to 30 s. Raw files were analyzed via pLink 2.3.5 to identify cross-linked peptides.[84] Database was generated based on the protein complex used. FDR was set to 1 % and results were filtered by excluding crosslinks supported by only one cross-linked peptide spectrum match. The crosslinks were visualized using the webserver xiNET.[85]

Fluorescence microscopy of liposomes

For Microscopy the LSM 780 (Carl Zeiss) was used. μ-slides with 8-wells (Ibidi) were coated with BSA by incubating each well with 100 μl 5 mg/ml BSA followed by 3 washing steps with protein buffer (150 mM NaCl, 50 mM HEPES (pH 8.0), 0.5 mM TCEP,1 mM EDTA, pH 8, Osm. 380 mOsm). The wells were prepared for the addition of the GUVs with 200 μl of protein buffer. GUVs were added carefully with a tip-cut pipette. An appropriate window for microscopy was selected and indicated proteins were added to the wells. The pictures were processed with ImageJ-software.

Generation of GUVs

GUVs were formed by an adapted electroformation protocol as described before[86,87] in the VesiclePrepPro (Nanion). In brief, first a 2 mg/ml lipid mix was prepared. A rubber ring (Ø28 mm) was slightly coated with silicon and placed carefully on the center of the electrically conductive side of an ITO-plate. The ITO-plate was heated to 50°C on a heating plate. 7.5 μl of the lipid mixture was applied dropwise with a Hamilton syringe on the ITO-plate in the area surrounded by the rubber ring. Following the ITO-plate was placed in a vacuum chamber for 10 min to evaporate the residual organic solvent. The plate was inserted in the chamber and an electroformation buffer (240 mM sucrose, 50 mM HEPES (pH 8.0), Osm. 380 mOsmol) was added slowly on the lipids. A second ITO-plate was placed on top of the first ITO-plate with the electrically conductive side facing the lipids and the buffer. This way the chamber was sealed. The electroformation protocol used here consists of three phases: In phase 1 the peak-to-peak amplitude rises linearly from 0 to 2 V. During phase 2 it stays on 2 V for 2 h 55 min. In phase 3 the amplitude decreases to 0 V again in a 20 min period. The frequency is set to 10 Hz in phase 1 and 2. In phase 3 it decreases to 0 Hz linearly. The temperature is set across all three phases to 55 °C and as such above the phase-transition temperature of the lipid mix. After finishing the protocol, GUVs were harvested into 1.5 ml Eppendorf tubes. They were used immediately for microscopy.

DLS analysis

LUVs were prepared as described above. To mimic conditions of the lipid transfer experiment, 25 μM lipid concentration of donor liposomes and acceptor liposomes in the presence or absence of the indicated proteins except ATG2 were prepared in 200 μl buffer (50 mM HEPES (pH 8), 150 mM NaCl, 0.5 mM TCEP). A 72-well Terasaki-plate (Greiner bio-one), was prepared with a thin layer of liquid paraffin oil. 1 μl of each solution was added to the wells. The plate was measured with the SpectraLight 610 on automatic settings. For creating the diagrams, GraphPad Prism (GraphPad Software, Inc.) software was used.

Cell lines and cell culture

Wild-type and *atg13* KO MEFs containing an insertion of a gene-trap cassette in the *atg13* gene, and wild-type and *atg101* KO MEFs were kindly provided by Noboru Mizushima (Department of Biochemistry and Molecular Biology, Graduate School and Faculty of Medicine, University of Tokyo, Japan) and have previously been described.[27,69] HCT116 ATG9A-HA KI cells and HCT116 ATG9A-HA KI ATG9 KO or ATG101 KO or ATG13 KO cells were kindly provided by Joshua L. Andersen (Department of Chemistry and Biochemistry, Brigham Young University, Utah, US) and have previously been described.[26] Wild-type MEFs, *atg13* KO MEFs, *atg101* KO MEFs and corresponding transfectants generated in this study were cultured in high-glucose (4,5 g/L) DMEM (Gibco, #41965-039) supplemented with 10% FCS (Sigma-Aldrich, #F0804, LOT BCCB7649 and #F9665, LOT 0001655429), 100 U/ml penicillin and 100 μg/ml streptomycin (Gibco, #15140-122) at 37 °C and 5% CO_2 humidified atmosphere. HCT-116 cells were cultured in McCoy's 5A (1X) + GlutaMAX™-I (Modified Medium) (Gibco, #36600-021) supplemented with 10% FCS, 100 U/ml penicillin and 100 μg/ml streptomycin at 37 °C and 5% CO_2 humidified atmosphere. For amino acid starvation, cells were washed once with DPBS (Dulbecco's Phosphate-Buffered Saline, Gibco, #14190-094) and incubated for the indicated time points in EBSS (Earle's Balanced Salt Solution, Gibco, #24010-043).

Retroviral transduction

Generation of pMSCVpuro-HA-ATG13 has previously been described[88] pMXs-IP-3xHA-ATG101 was kindly provided by Noboru Mizushima (Department of Biochemistry and Molecular Biology, Graduate School and Faculty of Medicine, University of Tokyo, Japan). For generation of pMXs-IP empty vector control the sequence encoding 3xHA-ATG101 was excised by *NotI* (Thermo Fisher Scientific, #FD0595) digestion and the backbone was subsequently ligated using T4 ligase (Thermo Fisher Scientific, #EL0011). For generation of cDNAs encoding HA-ATG13_ΔSB (Δaa185-194) or 3xHA-ATG101_ΔN (Δaa2-12), site-directed mutagenesis was performed using the following primers: ATG13-ΔSB fwd, ATG13-ΔSB rev, ATG101-ΔN fwd, ATG101-ΔN rev. Additionally, constructs were generated containing cDNA encoding untagged ATG13 or ATG101 (wt or variant) by using following primers: HAdel_ATG101wt_fwd, HAdel_ATG101wt_rev, HAdel_ATG101-ΔN_fwd, HAdel_ATG101-ΔN_rev, HAdel_ATG13wt_fwd and HAdel_ATG13wt/ΔSB_rev. pMSCVblast-ATG101 was generated by cloning ATG101 cDNA from pMXs-IP-3xHA-ATG101 into pMSCVblast via Gibson Assembly. Following primers were used: ATG101_fwd, ATG101_rev, pMSCVblast_fwd and pMSCVblast_rev. For generation of cDNAs encoding ATG9A-HA-ΔN (Δaa2-42), ATG9A-HA-ΔC (Δaa809-839) and ATG9A-HA-P833A/P834A, site-directed mutagenesis was performed using pMSCVpuro-ATG9A-HA and the following primers: ATG9A-ΔN_fwd, ATG9A-ΔN_rev, ATG9A-ΔC_fwd, ATG9A-ΔC_rev, ATG9A-PAPA_fwd and ATG9A-PAPA_rev. Plat-E cells (kindly provided by Toshio Kitamura, Institute of Medical Science, University of Tokyo, Japan) were used as packaging cells, and were transfected with the pMSCV- or pMXs-IP-based retroviral expression vectors using FuGENE® 6 (Promega, #E2691). After 48 h, MEFs and HCT cells were incubated with the corresponding retroviral supernatants containing 3 μg/ml Polybrene (Sigma-Aldrich, #H9268-106 and Santa Cruz, #sc-134220) and selected in medium containing 2.5-3 μg/ml puromycin (InvivoGen, #ant-pr-1) or 10 μg/ml blasticidin (InvivoGen, #ant-bl-05).

Immunoblotting

Cells were harvested by scraping, washed once with ice-cold phosphate-buffered saline (PBS). For immunoblotting, cells were either lysed in standard ice-cold lysis buffer (20 mM Tris-HCl (pH 7.5), 150 mM NaCl, 0.5 mM EDTA, 1 % (v/v) Triton X-100, protease inhibitor cocktail [Roche, #58698000] and PhosSTOP [Roche, #04906837001]) or in ATG9A lysis buffer (20 mM Tris-HCl (pH 7.5), 150 mM NaCl, 5 mM EDTA, 0.3 % (v/v) Triton X-100, protease inhibitor cocktail and PhosSTOP)[26] for 30 min on ice. Lysates were clarified by centrifugation at 13,300 rpm for 15 min at 4 °C. Equal amounts of protein were determined by Bradford method. After adding Lämmli buffer, samples were either boiled at 95 °C or incubated for 2 h at room temperature because of thermal aggregation of ATG9. Samples were then subjected to SDS-PAGE. Proteins were then transferred to PVDF membranes (Millipore, #IPFL00010) and analyzed using the indicated primary antibodies and appropriate IRDye-conjugated secondary antibodies. Protein signals were detected using an Odyssey Infrared Imaging system (LI-COR Biosciences) and quantified using Image Studio Lite 5.2 (LI-COR Biosciences).

Immunofluorescence

Cells were seeded onto cover glasses (Marienfeld, Lauda-Königshofen, Germany) one or two days prior to stimulation. Cells were fixed in 4 % formaldehyde/DPBS for 15 min, permeabilized using 50 μg/ml Digitonin (Sigma Aldrich, #D141) for 5 min and blocked with 3% BSA (Roth, #8076) in DPBS for 30 min. Primary and secondary antibodies were diluted in 3% BSA/DPBS and incubated on samples for 2 h and for 30 min respectively. For ATG14-phospho staining cells were fixed in ice-cold methanol for 10 min at -20 °C and blocked and stained in 3 % BSA/DPBS containing 0.3% Triton X-100 (Roth, #3051). Finally, samples were washed once with DPBS containing 0.2% Tween 20 (Sigma-Aldrich, #P1379), stained with 1 μg/ml DAPI (Roth, #6335) for 10 min and embedded in ProLong Glass Antifade Mountant (Thermo Fisher Scientific, #P36980). Fluorescence imaging was performed using a Zeiss Axio Observer 7 fluorescence microscope equipped with colibri 7 as light source, a 90 HE LED filter cube, a 40x/1.4 Oil DIC M27 Plan-Apochromat objective (Zeiss, Jena, Germany) and ApoTome 2 (Zeiss, Jena, Germany). Images were taken by using ZEN 2.6 pro. DAPI, Alexa Fluor 488 and Alexa Fluor 647 were excited at 385 (20% LED intensity), 475 (80% LED intensity) and 630 nm (80% LED intensity), respectively. The exposure times were as following: DAPI: 7 ms; LC3 (AF488): 50 ms; ATG16L (AF488): 150 ms;

FIP200 (AF488): 120 ms; pATG14 (AF647): 800 ms; and WIPI2 (AF647): 600 ms. Confocal imaging was performed using a Zeiss LSM 880 Airyscan inverse confocal laser scanning microscope (Zeiss, Jena, Germany) equipped with a 63x/1.4 Oil DIC M27 Plan-Apochromat objective. Images were taken by using ZEN black at a scan speed of 1.10 μs and a sampling rate of 956x956 pixel, with the pinhole at 1 AU. DAPI, Alexa Fluor 488 and Alexa Fluor 647 were excited at 405, 488 and 633 nm respectively. Emission of DAPI fluorescence was detected in a range of 410-459 nm, emission of Alexa Fluor 488 in a range of 493-561 nm and emission of Alexa Fluor 647 in a range of 645-745 nm. Pixel intensity profiles of areas indicated by dashed red arrows were measured with ZEN lite 3.7 and are depicted in bar graphs. Quantifications of images were performed with ImageJ 1.53t.

QUANTIFICATION AND STATISTICAL ANALYSIS

All lipid transfer and scramblase experiments were done in independent triplicates. Comparisons among different variants were determined by one-way analysis of variances (ANOVA), followed by Tukey's multiple comparisons test. Student's t-test was used for 2-group comparisons. The error bars of these experiments indicate the standard error. P values < 0.05 were considered statistically significant. For immunoblotting, the density of each protein band was divided by the average density of all bands of this protein. The ratios were normalized to the loading control (for phosphorylated proteins, the phosphorylation signal was further normalized to the respective total protein), and fold changes were calculated by dividing each normalized ratio by the average of the ratios of the control line (n=3). The results are shown as mean + standard deviation. For immunofluorescence, evaluation of number and area of puncta was performed in ImageJ 1.53t. To determine the number of puncta per cell a ratio of puncta to cell nuclei was calculated. The ratio of puncta to cell nuclei of 20 images of three independent experiments is depicted in an interleaved box and whiskers plot (Tukey style). At least 500 cells per condition were analyzed. Macros used for quantification are provided in Table S2. Statistical analysis was performed using two-way ANOVA (corrected by Tukey's multiple comparisons test). For Figures 3A and 3B and for S9C and S9D, statistical analysis was performed using ordinary two-way ANOVA (corrected by Tukey's multiple comparisons test). For Figure S9B, statistical analysis was performed using ordinary one-way ANOVA (corrected by Dunnett's multiple comparisons test). Compared treatments or cell lines are indicated in the corresponding bar diagrams. P values < 0.05 were considered statistically significant. All statistical data were calculated with GraphPad Prism (version 9.0.0).